

Exploring the Fidelity of Flux Qubit Measurement in Different Bases via Quantum Flux Parametron

Yanjun Ji,^{1,*} Susanna Kirchhoff,^{1,2} and Frank K. Wilhelm^{1,2,†}

¹*Institute for Quantum Computing Analytics (PGI-12),
Forschungszentrum Jülich, 52045 Jülich, Germany*

²*Theoretical Physics, Saarland University, 66123 Saarbrücken, Germany*

(Dated: October 29, 2025)

High-fidelity qubit readout is a fundamental requirement for practical quantum computing systems. In this work, we investigate methods to enhance the measurement fidelity of flux qubits via a quantum flux parametron-mediated readout scheme. Through theoretical modeling and numerical simulations, we analyze the impact of different measurement bases on fidelity in single-qubit and coupled two-qubit systems. For single-qubit systems, we show that energy bases consistently outperform flux bases in achieving higher fidelity. In coupled two-qubit systems, we explore two measurement models: sequential and simultaneous measurements, both aimed at reading out a single target qubit. Our results indicate that the highest fidelity can be achieved either by performing sequential measurement in a dressed basis over a longer duration or by conducting simultaneous measurement in a bare basis over a shorter duration. Importantly, the sequential measurement model consistently yields more robust and higher fidelity readouts compared to the simultaneous approach. These findings quantify achievable fidelities and provide valuable guidance for optimizing measurement protocols in emerging quantum computing architectures.

I. INTRODUCTION

Quantum computers have the potential to efficiently solve computational problems that are intractable for classical computers. Among the various physical implementations, superconducting qubits [1, 2] stand out due to their scalability and compatibility with existing semiconductor fabrication techniques. Josephson junctions, composed of two superconductors separated by a thin insulating barrier, are essential components in constructing diverse qubit types, including charge [3, 4], phase [5], flux [6, 7], and transmon qubits [8]. Flux qubits, in particular, show promise for quantum information processing due to their long coherence times [9]. Furthermore, accurate and reliable qubit readout is crucial for practical quantum technologies. The properties and readout schemes of flux qubits have been extensively explored [10–15]. A widely used approach is dispersive measurement, which involves coupling superconducting qubits to microwave resonators [16] and has been experimentally validated [17–19]. Additionally, the quantum flux parametron (QFP) [20] has emerged as a notable candidate for qubit readout due to its high sensitivity and low power consumption [21]. Its application as an isolator and amplifier within the readout circuit has been shown, enabling fast and high fidelity measurements [22]. Despite these advancements, measurement fidelity remains influenced by various factors, with the choice of the appropriate measurement basis being a critical consideration [23, 24].

The measurement postulate in its simplest form states that the measurement basis is determined by the detector

[25]. In practice, this is often realized only if this basis coincides with the energy eigenbasis of the measured system, leading to a quantum nondemolition (QND) measurement. However, if the measurement basis does not coincide with the energy eigenbasis and the measurement is system-dominated, spurious transitions occur, and the measurement loses contrast. Conversely, the regime where the detector dictates the measurement basis is referred to as a detector-dominated scenario. Specifically for mid-anneal measurements in adiabatic quantum computing, it would be highly desirable to measure flux qubits in a detector-dominated scenario [26].

In this work, we propose a QFP-mediated measurement scheme and identify the measurement basis yielding the closest projection. Through theoretical analysis and numerical simulations, we evaluate the performance of different measurement bases, including flux, energy, bare, and dressed bases, in both single and coupled qubit systems. Additionally, we compare sequential and simultaneous measurements in coupled systems to determine their effectiveness in reading out a single target qubit. Our comprehensive study provides deeper insight into measurement processes and highlights new scenarios that extend beyond the conventional system-dominated regime. This optimization advances progress toward achieving high-fidelity measurements of flux qubits, which is crucial for developing large-scale quantum computers. Moreover, our findings have the potential to enhance measurement fidelity in near-term quantum devices [27] and improve the resilience of quantum algorithms [28, 29], paving the way for more reliable quantum information processing.

This paper is organized as follows. Section II provides background on QFPs, dispersive readout of qubits, and the measurement principle. Section III focuses on the measurement of a single flux qubit using a QFP-mediated

* y.ji@fz-juelich.de

† f.wilhelm-mauch@fz-juelich.de

readout scheme, comparing fidelity across different measurement bases. Section IV extends this analysis to coupled flux qubit systems, examining both sequential and simultaneous measurement strategies. Finally, Sec. V discusses the findings and concludes the paper.

II. PRELIMINARIES

A. Quantum flux parametron

The QFP is a controllable rf-SQUID (radio-frequency superconducting quantum interference device) [30] characterized by a small inductance, large capacitance, and a significantly higher critical current compared to a flux qubit [20]. This configuration results in a larger tunnel barrier, suppressing tunnel coupling and enhancing state stability against high-frequency radiation during readout [31]. Integrating a QFP between a flux qubit and its resonator offers two key advantages [22]: (1) amplification of the current signal, enabling more sensitive readout of qubit state; and (2) isolation of qubit from the resonator, effectively suppressing crosstalk that can degrade measurement accuracy.

The Hamiltonian describing the QFP and its interaction with a coupled flux qubit is given by [31, 32]

$$\hat{H}_{\text{qfp}} = \frac{\hat{Q}^2}{2C} + \frac{\left(\hat{\Phi} - \Phi_z^{\text{qfp}}\right)^2}{2L} - E_J \cos\left(\frac{\pi\Phi_x^{\text{qfp}}}{\Phi_0}\right) \cos\left(\frac{2\pi\hat{\Phi}}{\Phi_0}\right), \quad (1)$$

where \hat{Q} is canonical conjugate to $\hat{\Phi}$, C is the sum of two junction capacitances, and L is the inductance of the large loop. The magnetic flux induced by the flux qubit, denoted as Φ_z^{qfp} , is given by $\Phi_z^{\text{qfp}} = M_q I_p^q = M_q |I_p^q| \hat{\sigma}_z$, where M_q is the mutual inductance between the flux qubit and QFP, often referred to as coupling inductance, and I_p^q is the persistent current of qubit, which takes values $\pm |I_p^q|$ depending on the qubit state. $\hat{\sigma}_z$ is the Pauli Z operator, which represents a qubit state in the computational basis, with eigenvalues of ± 1 corresponding to two persistent current states of the flux qubit. Φ_0 denotes the magnetic flux quantum, while Φ_x^{qfp} corresponds to the external flux of QFP's small compound Josephson-junction (CJJ) loop. $E_J = \Phi_0 I_p^{\text{qfp}} / 2\pi$ represents Josephson energy, where I_p^{qfp} is the persistent current of the QFP. The QFP's small CJJ loop governs the energy barrier of the potential, while the large main loop, where the persistent current is generated, controls the symmetry of the potential [31, 32]. By slowly and adiabatically raising the magnetic flux in the small CJJ loop (Φ_x^{qfp}), the barrier of potential energy is raised, and its potential energy gradually transitions from monostable to bistable. This process, known as annealing, latches the final state of the flux qubit into the corresponding QFP. In the monostable state, the QFP functions as a resonator, whereas in the bistable state, it operates as a qubit.

Neglecting constant terms, the Hamiltonian can be reformulated in terms of standard dimensionless parameters [33] as

$$\hat{H}_{\text{qfp}} = E_L \left(4\xi^2 \frac{\hat{q}^2}{2} + \frac{\hat{\varphi}^2}{2} + \beta_L (\Phi_x^{\text{qfp}}) \cos \hat{\varphi} - \lambda \hat{\varphi} \hat{\sigma}_z \right), \quad (2)$$

where $E_L = \phi_0^2 / L$ is the inductive energy, $\phi_0 = \Phi_0 / (2\pi)$ is the reduced flux quantum, and $\xi = e/\phi_0 \sqrt{L/C}$ is the characteristic impedance. The operators are defined as $\hat{q} = \hat{Q}/(2e)$ and $\hat{\varphi} = \pi + \hat{\Phi}/\phi_0$. Similarly, $\varphi_z^{\text{qfp}} = \pi + \Phi_z^{\text{qfp}}/\phi_0$. Note that the definitions of $\hat{\varphi}$ and φ_z^{qfp} , with the π phase shift, result in a sign flip in front of $\beta_L (\Phi_x^{\text{qfp}}) \cos \hat{\varphi}$. The coupling term is given by $\lambda = M_q |I_p^q| / \phi_0$ and the screening parameter $\beta_L (\Phi_x^{\text{qfp}})$ is defined as

$$\beta_L (\Phi_x^{\text{qfp}}) = \frac{E_J}{E_L} \cos\left(\frac{\pi\Phi_x^{\text{qfp}}}{\Phi_0}\right) = \frac{I_p^{\text{qfp}} L}{\phi_0} \cos\left(\frac{\pi\Phi_x^{\text{qfp}}}{\Phi_0}\right). \quad (3)$$

The dimensionless potential $U(\varphi)$, given by

$$U(\varphi) = \frac{\hat{\varphi}^2}{2} + \beta_L (\Phi_x^{\text{qfp}}) \cos \hat{\varphi} - \lambda \hat{\varphi} \hat{\sigma}_z, \quad (4)$$

can be expanded around its minimum $\pm \varphi_p$, which satisfies $\frac{\partial U}{\partial \varphi}|_{\varphi=\pm\varphi_p} = 0$, where φ_p denotes the absolute value of the position of the potential minimum. By introducing the standard annihilation \hat{a} and creation \hat{a}^\dagger operators of the harmonic oscillator [34] and approximating the potential around its minimum [10], the Hamiltonian becomes

$$\hat{H}_{\text{qfp}} / E_L = \Omega \hat{a}^\dagger \hat{a} + \Omega \sqrt{\frac{m\Omega}{2}} \varphi_p (\hat{a}^\dagger + \hat{a}) \hat{\sigma}_z, \quad (5)$$

where $\Omega = 2\xi \sqrt{1 - \beta_L (\Phi_x^{\text{qfp}}) \cos(\varphi_p)}$ and $m = 1 / (2\xi)^2$.

B. Dispersive readout

After QFP annealing, the flux qubit signal is entangled with the corresponding displaced ground states or pointer states of the QFP [10], allowing the total system to be described by an efficient flux qubit Hamiltonian. More details can be found in Sec. III. The flux qubit signal is then read out by coupling the QFP to a resonator, with their interaction modeled as dipole coupling, resulting in a fully off-diagonal interaction, described by the Rabi Hamiltonian

$$\hat{H}_{\text{Rabi}} = \frac{\omega_q}{2} \hat{\sigma}_z + \omega_r \left(\hat{a}^\dagger \hat{a} + \frac{1}{2} \right) + g (\hat{a} + \hat{a}^\dagger) \hat{\sigma}_x, \quad (6)$$

where \hbar is set to 1, g is the coupling strength between the QFP and resonator, and ω_q and ω_r are the frequencies of QFP and resonator, respectively. The Pauli X matrix can be written as $\hat{\sigma}_x = \hat{\sigma}_+ + \hat{\sigma}_-$, where the raising and

lowering operators are defined as $\hat{\sigma}_{\pm} = \frac{1}{2}(\hat{\sigma}_x \pm i\hat{\sigma}_y)$ with $\hat{\sigma}_y$ being the Pauli Y matrix.

We transform \hat{H}_{Rabi} into a rotating frame by applying a unitary transformation

$$\hat{U}_r = \exp(i\omega_r t\hat{a}^\dagger \hat{a} - i\omega_q t\hat{\sigma}_z/2), \quad (7)$$

yielding

$$\tilde{\hat{H}}_{\text{Rabi}} = \hat{U}_r \hat{H}_{\text{Rabi}} \hat{U}_r^\dagger + i\dot{\hat{U}}_r \hat{U}_r^\dagger. \quad (8)$$

Using the Baker-Campbell-Hausdorff formula, we obtain

$$\begin{aligned} \tilde{\hat{H}}_{\text{Rabi}} = g & \left[\hat{a}\hat{\sigma}_+ e^{i(\omega_q - \omega_r)} + \hat{a}^\dagger \hat{\sigma}_- e^{i(\omega_r - \omega_q)} \right. \\ & \left. + \hat{a}\hat{\sigma}_- e^{-i(\omega_q + \omega_r)} + \hat{a}^\dagger \hat{\sigma}_+ e^{i(\omega_q + \omega_r)} \right]. \end{aligned} \quad (9)$$

Under the rotating wave approximation (RWA), where $(\omega_q + \omega_r) \gg \{g, |\omega_q - \omega_r|\}$, two fast oscillating terms can be neglected. Transforming back into the Schrödinger picture, the system is described by the well-known Jaynes-Cummings Hamiltonian [35], given by

$$\hat{H}_{\text{JC}} = \frac{\omega_q}{2} \hat{\sigma}_z + \omega_r \left(\hat{a}^\dagger \hat{a} + \frac{1}{2} \right) + g (\hat{\sigma}_+ \hat{a} + \hat{\sigma}_- \hat{a}^\dagger). \quad (10)$$

Diagonalizing the Hamiltonian in the subspace $\{|g, n+1\rangle, |e, n\rangle\}$ yields the eigenvalues

$$E_{\pm, n} = \omega_r \left(n + \frac{1}{2} \right) \pm \frac{1}{2} \sqrt{\delta^2 + 4g^2(n+1)}, \quad (11)$$

where $\delta = \omega_q - \omega_r$ is the detuning between the QFP and resonator frequencies. The corresponding eigenstates are

$$\begin{aligned} |+, n\rangle &= \cos\left(\frac{\theta_n}{2}\right) |e, n\rangle + \sin\left(\frac{\theta_n}{2}\right) |g, n+1\rangle, \\ |-, n\rangle &= -\sin\left(\frac{\theta_n}{2}\right) |e, n\rangle + \cos\left(\frac{\theta_n}{2}\right) |g, n+1\rangle, \end{aligned} \quad (12)$$

where the mixing angle θ_n is defined as $\tan(\theta_n) = 2g\sqrt{n+1}/\delta$. These eigenstates are referred to as *dressed states* in quantum optics and atomic physics, while $|g, n+1\rangle$ and $|e, n\rangle$ are *bare states*.

Under dispersive conditions, where $\omega_r \neq \omega_q$ and $g \ll |\delta|$, resonant photon absorption or emission is absent. Within this regime, we can approximate the Jaynes-Cummings Hamiltonian as [16, 36]

$$\hat{H}_{\text{disp}} = (\omega_r + \chi\hat{\sigma}_z) \left(\hat{a}^\dagger \hat{a} + \frac{1}{2} \right) + \frac{\omega_q}{2} \hat{\sigma}_z, \quad (13)$$

where $\chi = g^2/\delta$ is the dispersive shift. Notably, the first term reveals that the effective resonator frequency shifts depending on the QFP state. Consequently, it is possible to perform a QND measurement of the QFP by monitoring microwave transmission near the resonator frequency.

C. Measurement principle

We employ the single-qubit dispersive readout methodology in the presence of two-qubit coupling, as outlined in Ref. [23], to investigate how measurement speed and power influence the effective measurement basis and its deviation from the conventional computational basis. The measurement of qubit states proceeds as follows [23]. First, the resonator is initialized in a coherent state $|\alpha\rangle$ with α being real and positive. Subsequently, the resonator interacts with one of the qubits for a time interval $t_d = \pi/2|\chi|$, which is described by the time-evolution operator $U(t) = e^{-iHt}$. Afterward, the resonator is read out via a positive operator-valued measure (POVM) with elements

$$E_{\pm} = \frac{1}{\pi} \int_{\Omega_{\pm}} d^2\beta |\beta\rangle \langle \beta|, \quad (14)$$

where $E_+ + E_- = \mathbb{1}$, and integrals are over coherent states in lower ($\Omega_{\text{sgn}(\chi)}$) and upper half-plane ($\Omega_{-\text{sgn}(\chi)}$). Finally, the resonator is measured.

The associated superoperator describing the measurement outcome on an initial two-qubit state ρ is given by

$$\mathcal{E}_{\pm}(\rho) = \text{tr}_{\text{res}} \mathbb{1} \otimes E_{\pm} U(t_d) \rho \otimes |\alpha\rangle \langle \alpha| \hat{U}^\dagger(t_d). \quad (15)$$

Expanding this in terms of resonator Fock states $|n\rangle$ and $|m\rangle$, we have

$$\mathcal{E}_{\pm}(\rho) = \sum_{n,m=0}^{\infty} g_{\pm}(m, n) \langle n| U(t_d) |n\rangle \rho \langle m| \hat{U}^\dagger(t_d) |m\rangle, \quad (16)$$

where

$$g_{\pm}(m, n) = e^{-\alpha^2} \left(\frac{\alpha^{2n}}{2n!} \mp \frac{i}{\pi} \frac{\alpha^{n+m} \Gamma(\frac{m+n}{2} + 1)}{m! n! (m-n)} \text{odd}(m-n) \right) \quad (17)$$

with

$$\text{odd}(n) = \begin{cases} 1, & n \text{ is odd} \\ 0, & \text{otherwise.} \end{cases} \quad (18)$$

In practical scenarios, the summation over n and m is truncated at a finite maximum value N to ensure computational feasibility while neglecting the insignificant contributions of higher Fock states.

III. ANALYSIS OF SINGLE FLUX QUBIT MEASUREMENT

This section explores the measurement process for a single flux qubit mediated by a QFP. Figure 1 provides a schematic overview of the approach. We first examine the coupled system of flux qubit and QFP through numerical simulation to evaluate the fidelity in the flux and energy bases. Then, we assume that the adiabatic QFP annealing is successful and the flux qubit state is latched

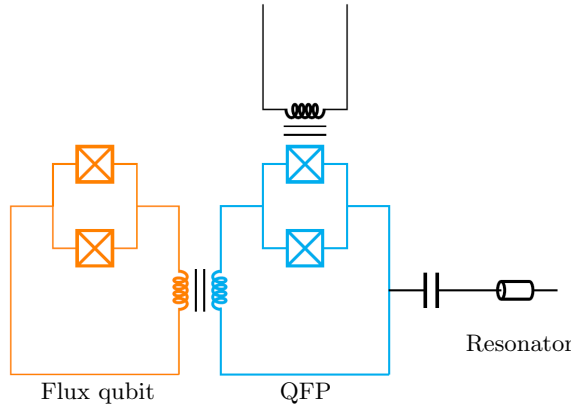


FIG. 1. Quantum flux parametron (QFP)-mediated scheme for measuring a single flux qubit. The flux qubit is coupled to a QFP. After QFP annealing, the qubit state is latched into the QFP, which is then read out using a resonator.

into the QFP. The coupled system is thus described by an effective flux qubit Hamiltonian. Finally, we use a resonator to read out the qubit state latched in the QFP.

A. QFP annealing

Building on the analysis in Sec. II A, the total Hamiltonian describing the coupled system of flux qubit and QFP is given by

$$\hat{H} = \tilde{\Omega} \hat{a}^\dagger \hat{a} + \tilde{g} \varphi_p (\hat{a}^\dagger + \hat{a}) \hat{\sigma}_z - \frac{1}{2} (\epsilon_q \hat{\sigma}_z + \Delta_q \hat{\sigma}_x), \quad (19)$$

where ϵ_q and Δ_q are the energy spacing and tunneling energy of the flux qubit, respectively. The effective frequency $\tilde{\Omega}$ is defined as

$$\tilde{\Omega} = E_L \Omega = 2\xi \phi_0^2 / L \sqrt{1 - \beta_L (\Phi_x^{\text{qfp}}) \cos(\varphi_p)}. \quad (20)$$

The corresponding effective coupling strength \tilde{g} is then determined by $\tilde{g} = \tilde{\Omega} \sqrt{m \tilde{\Omega} / (2E_L)}$. If the two junctions in the QFP are identical, the total critical current of the QFP is $I_q^{\text{qfp}} = 2I_c^{\text{qfp}}$, where I_c^{qfp} is the critical current of each junction in the small CJJ loop. Then we have

$$\beta_L (\Phi_x^{\text{qfp}}) = \frac{4\pi L I_c^{\text{qfp}}}{\Phi_0} \cos\left(\frac{\pi \Phi_x^{\text{qfp}}}{\Phi_0}\right). \quad (21)$$

Through adiabatic QFP annealing, the flux qubit and QFP evolve into an entangled state [10, 37]

$$(\alpha |0\rangle + \beta |1\rangle) \otimes |0\rangle \longrightarrow (\alpha_{\text{eff}} |0, L\rangle + \beta_{\text{eff}} |1, R\rangle), \quad (22)$$

where the flux qubit state becomes entangled with the pointer states of the QFP. The system is then described by an effective flux qubit Hamiltonian (further details

are provided in Appendix A 1). Under the Gaussian approximation, the fidelity measured in the flux basis for a measurement time interval T is given by [10]

$$\mathcal{F}_T = \Phi\left(\frac{\varphi_p(T)}{\hat{\sigma}(T)}\right), \quad (23)$$

where $\hat{\sigma}(T) = [\sqrt{1 - \beta_L(T) \cos(\varphi_p(T))} / \xi]^{-1/2}$ is the standard deviation of Gaussian wave packet, $\varphi_p(T)$ is the positive position of double-well potential minimum at time T , and $\Phi(x) = \frac{1}{\sqrt{2\pi}} \int_{-\infty}^x e^{-t^2/2} dt$ is the normal cumulative distribution function.

In the qubit energy eigenbasis, the positive position of potential minimum is given by $\tilde{\varphi}_p(T) = [\cos(\theta_q) - i \sin(\theta_q)] \varphi_p(T)$, where θ_q is defined as $\tan(\theta_q) = \Delta_q / \epsilon_q$, and the fidelity becomes

$$\tilde{\mathcal{F}}_T = \Phi\left(\frac{\tilde{\varphi}_p(T)}{\tilde{\hat{\sigma}}(T)}\right), \quad (24)$$

where $\tilde{\hat{\sigma}}(T) = [\sqrt{1 - \beta_L(T) \cos(\tilde{\varphi}_p(T))} / \xi]^{-1/2}$.

Figure 2 illustrates the fidelity evolution as a function of t/t_{qfp} and β_{max} , where t_{qfp} is the total annealing time. As shown in Fig. 2(a), the fidelity consistently increases over time in both flux and energy bases, saturating near the completion of QFP annealing process. At the full annealing time t_{qfp} , the flux qubit state is latched into the QFP ground state, achieving fidelities approaching unity. Moreover, the energy basis outperforms the flux basis by achieving higher fidelity. As illustrated in Fig. 2(b), the fidelity in the energy basis reaches its maximum at $\beta_{\text{max}} = 1.4$, while in the flux basis it peaks at a slightly higher value, $\beta_{\text{max}} = 1.6$. For β_{max} values below these optima, the potential barrier during QFP annealing is insufficient, resulting in less distinguishable states and subsequently lower fidelities. These results demonstrate that adiabatic QFP annealing can successfully latch the flux qubit state into the QFP in both the flux and energy bases, with higher efficiency observed in the energy basis.

B. Measurement in different bases

After annealing, the resulting coupled system of flux qubit and QFP is described by an effective flux qubit Hamiltonian [37] (see Appendix A 1 for further details)

$$\hat{H}_{\text{eff}} = -\frac{1}{2} (\epsilon_q \hat{\sigma}_z + \Delta_{\text{eff}} \hat{\sigma}_x) \quad (25)$$

where Δ_{eff} is the effective detuning, which is reduced compared to the original detuning Δ_q of the flux qubit. This reduction is characterized by a Franck-Condon-type factor of $e^{-\eta}$ ($\Delta_{\text{eff}} = \Delta_q e^{-\eta}$), where η is determined by the specific QFP design [37].

The QFP is then read out via a coupled resonator, as demonstrated in Fig. 1. The Hamiltonian of the system

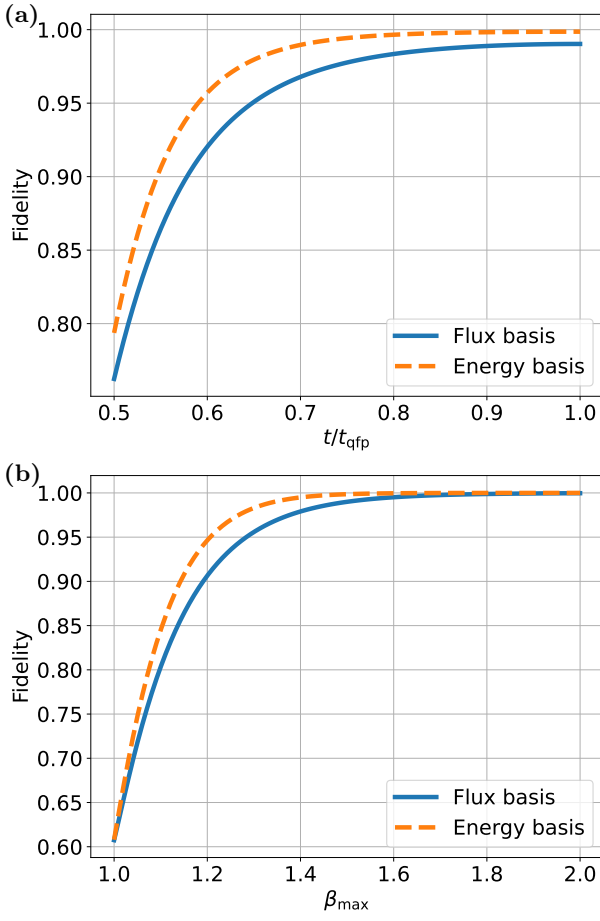


FIG. 2. QFP annealing fidelity as a function of (a) normalized annealing time t/t_{qfp} for $\beta_{\text{max}} = 1.5$ and (b) maximal screening parameter β_{max} at the total annealing time t_{qfp} . Fidelity is evaluated in both flux and energy bases for $\Delta_q/\epsilon_q = 4$ and $\xi = 0.4$.

is described by

$$\hat{H} = -\frac{1}{2}(\epsilon_q \hat{\sigma}_z + \Delta_{\text{eff}} \hat{\sigma}_x) + \omega_r \hat{a}^\dagger \hat{a} + g \hat{\sigma}_z (\hat{a} + \hat{a}^\dagger), \quad (26)$$

where ω_r is resonator frequency and g is coupling strength. Transforming into the qubit energy eigenbasis, we obtain

$$\begin{aligned} \tilde{H} = & -\frac{\omega_{\text{eff}}}{2} \tilde{\sigma}_z + g \left[\cos(\theta_{\text{eff}}) \tilde{\sigma}_z - \sin(\theta_{\text{eff}}) \tilde{\sigma}_x \right] (\hat{a}^\dagger + \hat{a}) \\ & + \omega_r \hat{a}^\dagger \hat{a}, \end{aligned} \quad (27)$$

where $\tilde{\sigma}_z$ is the Pauli Z operator in the qubit eigenbasis, $\omega_{\text{eff}} = \sqrt{\epsilon_q^2 + \Delta_{\text{eff}}^2}$, and θ_{eff} is defined as $\tan(\theta_{\text{eff}}) = \Delta_{\text{eff}}/\epsilon_q$. Under the RWA, the Hamiltonian becomes

$$\begin{aligned} \tilde{H} = & -\frac{\omega_{\text{eff}}}{2} \tilde{\sigma}_z + \omega_r \hat{a}^\dagger \hat{a} + g \cos(\theta_{\text{eff}}) \tilde{\sigma}_z (\hat{a}^\dagger + \hat{a}) \\ & - g \sin(\theta_{\text{eff}}) (\hat{a} \tilde{\sigma}_+ + \hat{a}^\dagger \tilde{\sigma}_-). \end{aligned} \quad (28)$$

Applying the displacement operator $\hat{D}(\alpha) = \exp(\alpha \hat{a}^\dagger - \alpha^* \hat{a})$ and choosing $\alpha = -g \cos(\theta_{\text{eff}}) \tilde{\sigma}_z / \omega_r$, we obtain

$$\tilde{H} = -\frac{\omega_{\text{eff}}}{2} \tilde{\sigma}_z + \omega_r \hat{a}^\dagger \hat{a} - g \sin(\theta_{\text{eff}}) (\hat{a} \tilde{\sigma}_+ + \hat{a}^\dagger \tilde{\sigma}_-). \quad (29)$$

In the dispersive regime with $\delta = \omega_{\text{eff}} - \omega_r \neq 0$ and $g \sin(\theta_{\text{eff}}) \ll |\delta|$, the Hamiltonian becomes

$$\tilde{H} = -\frac{\delta}{2} \tilde{\sigma}_z - g \sin(\theta_{\text{eff}}) (\hat{a} \tilde{\sigma}_+ + \hat{a}^\dagger \tilde{\sigma}_-). \quad (30)$$

Finally, by applying a unitary transformation $\hat{U}_3 = \exp(\lambda (\hat{a} \tilde{\sigma}_+ - \hat{a}^\dagger \tilde{\sigma}_-))$ with $\lambda = g \sin(\theta_{\text{eff}})/\delta$, we derive the Hamiltonian in the energy basis up to the first order in λ

$$\tilde{H}_{(e)} = -\left[\frac{\delta}{2} + \chi \left(\hat{a}^\dagger \hat{a} + \frac{1}{2}\right)\right] \tilde{\sigma}_z, \quad (31)$$

where $\chi = g^2 \sin^2(\theta_{\text{eff}})/\delta$.

Transforming the Hamiltonian back into the flux basis, we obtain

$$\hat{H}_{(f)} = -\left[\frac{\delta}{2} + \chi \left(\hat{a}^\dagger \hat{a} + \frac{1}{2}\right)\right] [\cos(\theta_{\text{eff}}) \hat{\sigma}_z + \sin(\theta_{\text{eff}}) \hat{\sigma}_x]. \quad (32)$$

The state fidelity between two quantum states represented by density matrices ρ and σ is defined by [38]

$$F(\rho, \sigma) = \left(\text{Tr} \sqrt{\sqrt{\rho} \sigma \sqrt{\rho}} \right)^2. \quad (33)$$

For an initial state $|\psi_i\rangle = \alpha |0\rangle + \beta |1\rangle$, the measurement operator in Eq. (15) evolves it to $\mathcal{E}_\pm(\rho) |\psi_i\rangle$. Fidelity between the initial and final states is then given by $\mathcal{F} = \langle \psi_i | \mathcal{E}_\pm(\rho) | \psi_i \rangle$.

Figure 3 presents numerical results exploring measurement fidelity as a function of χt and α . In Fig. 3(a), we observe that increasing χt leads to a significant improvement in fidelity, reaching a maximum value at the measurement time $t = t_d$. This highlights the benefit of longer measurement durations for accurate state discrimination. Similar trends are observed for the resonator coherent state amplitude α in Fig. 3(b), where larger values of α yield improved achievable fidelities, while smaller values of α lead to reduced fidelities regardless of the measurement basis. Crucially, energy basis consistently outperforms flux basis across all χt and α values. This implies that with these parameters, the QFP measurements are closer to the energy basis than to the flux basis. Furthermore, as η increases, the difference between flux and energy basis decreases. As shown in Fig. 3, larger η enhances fidelity in the flux basis but leaves it unchanged in the energy basis. The underlying reason is that, as η increases, Δ_{eff} approaches zero, causing the flux basis to more closely approximate the energy basis.

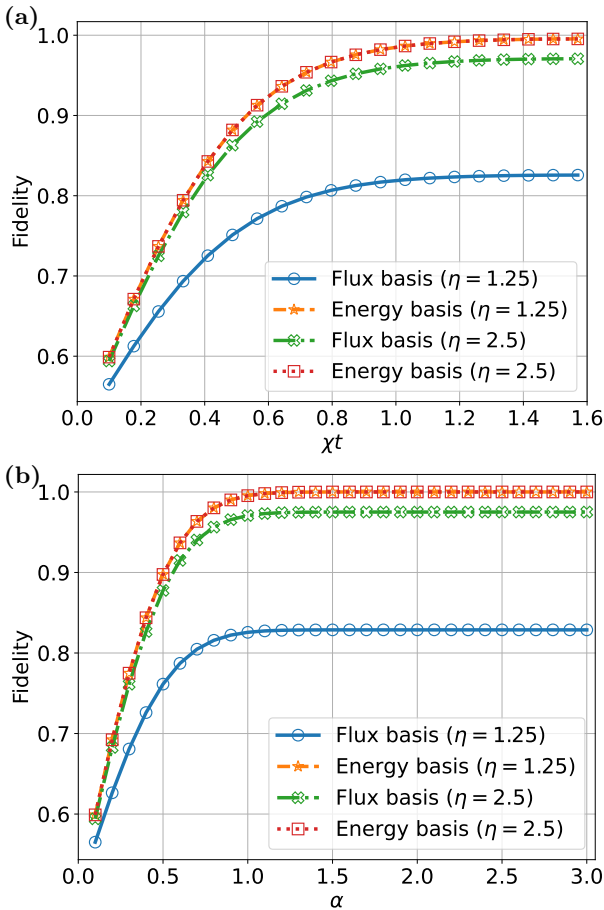


FIG. 3. Fidelity calculated using the Hamiltonian expressed in both flux and energy bases for $\eta = 1.25$ and $\eta = 2.5$, with $N = 27$, $\Delta_q/\epsilon_q = 4$, and $\delta/g = 8$. Fidelity as a function of (a) χt for $\alpha = 1$ and (b) α at the measurement time $t = t_d$.

IV. MEASUREMENT OF COUPLED FLUX QUBIT SYSTEM

In this section, we delve into a system of two coupled flux qubits denoted as q_1 and q_2 . Each qubit is coupled to a QFP: specifically, q_1 couples to QFP₁, and q_2 couples to QFP₂. Our primary objective is to read out the state of a single flux qubit q_2 in this coupled system. We aim to determine whether the QFP-mediated measurement ends up in a single- or two-qubit eigenbasis. Two distinct models are explored: sequential and simultaneous measurements. In the sequential measurement model, QFP₂ undergoes adiabatic annealing, while QFP₁ remains unaffected. After adiabatic QFP₂ annealing, the measurement of q_2 is performed using a resonator. In contrast, both QFP₁ and QFP₂ undergo adiabatic annealing simultaneously in the simultaneous measurement model. We conduct theoretical analysis and numerical simulations to assess the fidelity of q_2 under both measurement conditions.

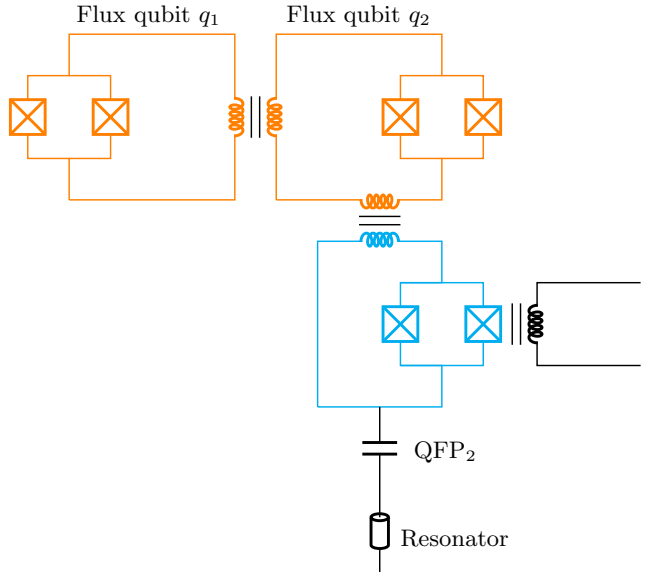


FIG. 4. Sequential measurement model. Two flux qubits q_1 and q_2 are coupled. QFP₂ undergoes adiabatic annealing to latch the state of q_2 . Subsequently, the state of QFP₂ is read out using a resonator.

A. Sequential measurement

The sequential measurement model is presented in Fig. 4. Before introducing the Hamiltonian, it is important to clarify the underlying assumptions. In particular, we consider a scenario where the first qubit, q_1 , remains essentially static or strongly biased, rendering its intrinsic dynamics negligible over the relevant timescales. Under these conditions, q_1 can be treated as a quasi-classical parameter, allowing its Hamiltonian to be omitted without compromising the essential physics. Retaining only the qubit-qubit interaction ensures that the influence of the first qubit on the second remains accurately captured, thereby yielding a simplified yet physically meaningful description of the system. Furthermore, we assume that adiabatic QFP₂ annealing has been successfully performed, with the state of q_2 fully latched into QFP₂. The focus then shifts to the readout process of QFP₂ using a resonator, accompanied by an analysis of fidelity across various bases. The total Hamiltonian in the flux basis is given by

$$\hat{H} = -\frac{1}{2}(\epsilon_2 \hat{\sigma}_2^z + \Delta_{\text{eff},2} \hat{\sigma}_2^x) + J \hat{\sigma}_1^z \hat{\sigma}_2^z + g \hat{\sigma}_2^z (\hat{a}^\dagger + \hat{a}) + \omega_r \hat{a}^\dagger \hat{a}, \quad (34)$$

where J is the coupling strength between two flux qubits, g represents coupling strength between q_2 and resonator, and ω_r is resonator frequency. In Appendix A 2, we demonstrate that J is not renormalized.

In the rotating frame with frequency ω_r , the Hamiltonian is

nian in q_2 energy basis becomes

$$\begin{aligned}\tilde{H} = & -\frac{\delta_{\text{eff},2}}{2}\tilde{\sigma}_2^z + J\hat{\sigma}_1^z \left[\cos(\theta_{\text{eff},2})\tilde{\sigma}_2^z - \sin(\theta_{\text{eff},2})\tilde{\sigma}_2^x \right] \\ & + g \left[\cos(\theta_{\text{eff},2})\tilde{\sigma}_2^z - \sin(\theta_{\text{eff},2})\tilde{\sigma}_2^x \right] (\hat{a}^\dagger + \hat{a}),\end{aligned}\quad (35)$$

where $\theta_{\text{eff},2}$ is defined as $\tan(\theta_{\text{eff},2}) = \Delta_{\text{eff},2}/\epsilon_2$ and $\delta_{\text{eff},2} = \omega_{\text{eff},2} - \omega_r$ is effective frequency detuning with $\omega_{\text{eff},2} = \sqrt{\epsilon_2^2 + \Delta_{\text{eff},2}^2}$. Applying the displacement operator $\hat{D}(\alpha)$ with $\alpha = -g \cos(\theta_{\text{eff},2})\tilde{\sigma}_2^z/\omega_r$, we obtain the Hamiltonian under the RWA as

$$\begin{aligned}\tilde{H} = & -\frac{\delta_{\text{eff},2}}{2}\tilde{\sigma}_2^z + J\hat{\sigma}_1^z \left[\cos(\theta_{\text{eff},2})\tilde{\sigma}_2^z - \sin(\theta_{\text{eff},2})\tilde{\sigma}_2^x \right] \\ & - g \sin(\theta_{\text{eff},2}) \left(\hat{a}^\dagger \tilde{\sigma}_2^- + \hat{a} \tilde{\sigma}_2^+ \right).\end{aligned}\quad (36)$$

To eliminate the interaction term between q_2 and resonator, we apply a unitary operator $\hat{U} = \exp(\lambda(\hat{a}\tilde{\sigma}_2^+ - \hat{a}^\dagger\tilde{\sigma}_2^-))$ with $\lambda = g \sin(\theta_{\text{eff},2})/\delta_{\text{eff},2}$, to Eq. (36). This transformation yields the Hamiltonian in the q_2 energy basis

$$\tilde{H}_{(e_2)} \approx -\frac{\delta_{\text{eff2,n}}}{2}\tilde{\sigma}_2^z + J\hat{\sigma}_1^z \left[\cos(\theta_{\text{eff},2})\tilde{\sigma}_2^z - \sin(\theta_{\text{eff},2})\tilde{\sigma}_2^x \right],\quad (37)$$

where $\delta_{\text{eff2,n}} = \delta_{\text{eff},2} + \chi(2\hat{n} + 1)$ with $\hat{n} = \hat{a}^\dagger\hat{a}$ and dispersive shift $\chi = g^2 \sin^2(\theta_{\text{eff},2})/\delta_{\text{eff},2}$.

To study the fidelity in different bases, we express the Hamiltonian (Eq. (37)) in the flux basis as

$$\begin{aligned}\hat{H}_{(f)} \approx & -\frac{\hat{\delta}_{\text{eff2,n}}}{2} [\cos(\theta_{\text{eff},2})\hat{\sigma}_2^z + \sin(\theta_{\text{eff},2})\hat{\sigma}_2^x] \\ & + J\hat{\sigma}_1^z\hat{\sigma}_2^z.\end{aligned}\quad (38)$$

Similarly, the Hamiltonian can be further written in the q_1 energy basis (or q_1 - q_2 energy basis)

$$\begin{aligned}\tilde{H}_{(e)} \approx & -\frac{\hat{\delta}_{\text{eff2,n}}}{2}\tilde{\sigma}_2^z + J \left[\cos(\theta_1)\tilde{\sigma}_1^z - \sin(\theta_1)\tilde{\sigma}_1^x \right] \\ & \otimes \left[\cos(\theta_{\text{eff},2})\tilde{\sigma}_2^z - \sin(\theta_{\text{eff},2})\tilde{\sigma}_2^x \right],\end{aligned}\quad (39)$$

where θ_1 is defined as $\tan(\theta_1) = \epsilon_1/\Delta_1$ with energy spacing ϵ_1 and tunneling energy Δ_1 of q_1 . Then we can investigate the fidelity in different bases with the measurement operator

$$\mathcal{E}_\pm(\rho) = \text{tr}_{\text{res}} \text{tr}_{q_1} E_\pm U(t_d) \rho \otimes |\alpha\rangle\langle\alpha| \hat{U}^\dagger(t_d).\quad (40)$$

Compared to the previous case, we need to additionally trace out q_1 since we are only interested in the fidelity of q_2 .

Figure 5 displays the fidelity dependence on χt , α , and $J/(\omega_2 - \omega_1)$, where $\omega_1 = \sqrt{\epsilon_1^2 + \Delta_1^2}$. As shown in Fig. 5(a), the q_2 energy basis exhibits the highest overall fidelity, peaking at the measurement time $t = t_d/2$, and then displaying a slight decline. This behavior might be attributed to the interaction between q_1 and q_2 . Due

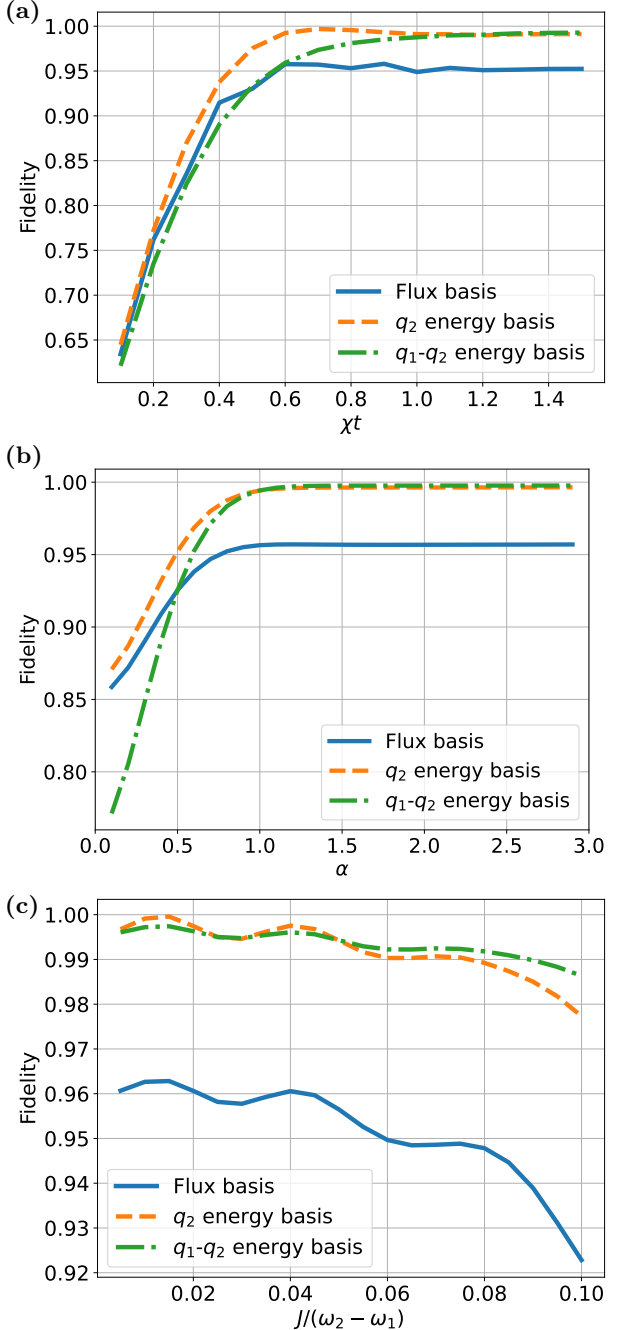


FIG. 5. Fidelity calculated using the Hamiltonian expressed in the flux basis, q_2 energy basis, and q_1 - q_2 energy basis with $N = 27$, $\eta = 1.25$, $\Delta_2/\epsilon_2 = 1$, and $\delta/g = 8$. Fidelity as a function of (a) χt for $J/(\omega_2 - \omega_1) = 0.05$ and $\alpha = 1$; (b) α for $J/(\omega_2 - \omega_1) = 0.05$ and $t = t_d$; and (c) $J/(\omega_2 - \omega_1)$ for $t = t_d$ and $\alpha = 1$.

to the dressed state formation, we measure the coupled system instead of q_2 individually. This distinction disappears only when the QND condition holds. Therefore, for longer measurement times, the q_1 - q_2 energy basis might be more appropriate. However, the q_1 - q_2 energy basis reaches maximum fidelity slower than the q_2 en-

ergy basis. Additionally, for shorter measurement times ($t \lesssim t_d/\pi$), the flux basis outperforms the q_1 - q_2 energy basis. At $\alpha \approx 1$, all bases achieve the maximum fidelity and remain constant, as shown in Fig. 5(b). However, both energy bases outperform the flux basis. A basis crossover between flux basis and q_1 - q_2 energy basis occurs around $\alpha \approx 0.5$, whereas the crossover between the two energy bases is less pronounced. This is potentially due to the chosen parameter values of $t = t_d$ (see Fig. 5(a)) and $J/(\omega_2 - \omega_1) = 0.05$ (see Fig. 5(c)). Finally, as shown in Fig. 5(c), we observe consistently higher fidelity in the q_2 and q_1 - q_2 energy bases compared to the flux basis. Stronger coupling between q_1 and q_2 leads to mutual influence during measurement, reducing fidelity. The basis crossover between two energy bases occurs at $J/(\omega_2 - \omega_1) \approx 0.05$, after which the q_1 - q_2 energy basis exhibits higher fidelity.

In the following, we delve into the validity of the RWA within both bare and dressed bases using the method described in Ref. [23]. Our investigation commences with the Hamiltonian operator expressed in the energy basis of the measured flux qubit (specifically, the q_2 energy basis, as given in Eq. (37)). We then extend our analysis to consider the Hamiltonian operator formulated in the energy basis of both flux qubits (q_1 - q_2 energy basis, detailed in Eq. (39)).

1. Energy basis of the measured flux qubit

To simplify the diagonalization of the Hamiltonian operator in the q_2 energy basis and improve mathematical clarity, we introduce the following substitution. Within the effective Hamiltonian $\hat{H}_{(e_2)}$, we replace the number operator $\hat{n} = \hat{a}^\dagger \hat{a}$ with its expectation value $n = \langle \hat{a}^\dagger \hat{a} \rangle$, resulting in $\hat{\delta}_{\text{eff2,n}} \rightarrow \delta_{\text{eff2,n}}$. This linearization is valid because we restrict our analysis to the flux qubit basis, excluding the resonator. In this specific basis, the operator $\hat{a}^\dagger \hat{a}$ effectively behaves as a constant. However, when returning to the general Hamiltonian operator, we must reinstate the operator, recovering $\delta_{\text{eff2,n}} \rightarrow \hat{\delta}_{\text{eff2,n}}$.

Diagonalization of Hamiltonian described in Eq. (37) yields the eigenvalues

$$E_{(e_2)} = \{ -\omega_{n-}, \omega_{n-}, -\omega_{n+}, \omega_{n+} \}, \quad (41)$$

where $\omega_{n\pm} = \sqrt{(\delta_{\text{eff2,n}}/2 \pm J_{zz})^2 + J_{zx}^2}$ with $J_{zz} = J \cos(\theta_{\text{eff},2})$ and $J_{zx} = J \sin(\theta_{\text{eff},2})$. The eigenstates are

given by

$$\begin{aligned} |\overline{00}\rangle &= \cos\left(\frac{\theta_{n-}}{2}\right) |\tilde{0}\tilde{0}\rangle + \sin\left(\frac{\theta_{n-}}{2}\right) |\tilde{0}\tilde{1}\rangle, \\ |\overline{01}\rangle &= -\sin\left(\frac{\theta_{n-}}{2}\right) |\tilde{0}\tilde{0}\rangle + \cos\left(\frac{\theta_{n-}}{2}\right) |\tilde{0}\tilde{1}\rangle, \\ |\overline{10}\rangle &= \cos\left(\frac{\theta_{n+}}{2}\right) |\tilde{1}\tilde{0}\rangle + \sin\left(\frac{\theta_{n+}}{2}\right) |\tilde{1}\tilde{1}\rangle, \\ |\overline{11}\rangle &= -\sin\left(\frac{\theta_{n+}}{2}\right) |\tilde{1}\tilde{0}\rangle + \cos\left(\frac{\theta_{n+}}{2}\right) |\tilde{1}\tilde{1}\rangle, \end{aligned} \quad (42)$$

with $\theta_{n\pm}$ satisfying $\tan(\theta_{n\pm}) = \mp J_{zx}/(\delta_{\text{eff2,n}}/2 \pm J_{zz})$. The relationship between the bare and dressed bases is described by

$$\begin{bmatrix} \hat{\sigma}_2^z + \hat{\sigma}_1^z \tilde{\sigma}_2^z \\ \hat{\sigma}_2^x + \hat{\sigma}_1^z \tilde{\sigma}_2^x \\ \hat{\sigma}_2^z - \hat{\sigma}_1^z \tilde{\sigma}_2^z \\ \hat{\sigma}_2^x - \hat{\sigma}_1^z \tilde{\sigma}_2^x \end{bmatrix} = A \begin{bmatrix} \tilde{\sigma}_2^z + \hat{\sigma}_1^z \tilde{\sigma}_2^z \\ \tilde{\sigma}_2^x + \hat{\sigma}_1^z \tilde{\sigma}_2^x \\ \tilde{\sigma}_2^z - \hat{\sigma}_1^z \tilde{\sigma}_2^z \\ \tilde{\sigma}_2^x - \hat{\sigma}_1^z \tilde{\sigma}_2^x \end{bmatrix} \quad (43)$$

with

$$A = \begin{bmatrix} \cos(\theta_{0-}) & -\sin(\theta_{0-}) & 0 & 0 \\ \sin(\theta_{0-}) & \cos(\theta_{0-}) & 0 & 0 \\ 0 & 0 & \cos(\theta_{0+}) & -\sin(\theta_{0+}) \\ 0 & 0 & \sin(\theta_{0+}) & \cos(\theta_{0+}) \end{bmatrix}. \quad (44)$$

Using these transformation relations, we obtain the Hamiltonian in the dressed basis

$$\begin{aligned} \bar{H}^{(2)} &= -\frac{\omega_{n-}}{2} [\cos(\theta_{n-} - \theta_{0-}) (\tilde{\sigma}_2^z + \hat{\sigma}_1^z \tilde{\sigma}_2^z) \\ &\quad + \sin(\theta_{n-} - \theta_{0-}) (\tilde{\sigma}_2^x + \hat{\sigma}_1^z \tilde{\sigma}_2^x)] \\ &\quad - \frac{\omega_{n+}}{2} [\cos(\theta_{n+} - \theta_{0+}) (\tilde{\sigma}_2^z - \hat{\sigma}_1^z \tilde{\sigma}_2^z) \\ &\quad + \sin(\theta_{n+} - \theta_{0+}) (\tilde{\sigma}_2^x - \hat{\sigma}_1^z \tilde{\sigma}_2^x)]. \end{aligned} \quad (45)$$

The validity of the RWA in the dressed basis requires

$$\left\| \frac{J_{zx} \chi (\hat{a}^\dagger \hat{a} + \frac{1}{2})}{(\hat{\delta}_{\text{eff2,n}}/2 \pm J_{zz}) (\delta_{\text{eff2,n}}/2 \pm J_{zz}) + J_{zx}^2} \right\| \ll 1. \quad (46)$$

Similarly, the RWA condition based on the bare basis is

$$\left\| \frac{J_{zx}}{(\hat{\delta}_{\text{eff2,n}}/2 \pm J_{zz})} \right\| \ll 1. \quad (47)$$

If the relationship

$$\left\| \chi \left(\hat{a}^\dagger \hat{a} + \frac{1}{2} \right) \right\| = \sqrt{(\delta_{\text{eff2,n}}/2 \pm J_{zz})^2 + J_{zx}^2} \quad (48)$$

holds, then the bare and dressed bases become indistinguishable for the system.

The fidelity in both bare and dressed bases is numerically investigated as a function of χt , α , and $J/(\omega_2 - \omega_1)$, as shown in Figs. 6(a-c) respectively. Figure 6(a) shows

that, for very short measurement times, the fidelity is low in both bases. At a measurement time of $t \approx t_d/2$, fidelity reaches its maximum value in both bases. Beyond this point, the fidelity in the dressed basis remains higher than that in the bare basis. However, in both bases, the fidelity gradually decreases as the measurement time further increases. As illustrated in Fig. 6(b), for small values of α , the bare basis performs better. A basis crossover occurs around $\alpha \approx 0.7$. Beyond this point, the fidelity in the dressed basis is higher. This implies that at a fixed measurement time (here, t_d), measuring gradually becomes better suited to the dressed basis as α increases. Figure 6(c) shows how the coupling strength between two flux qubits affects the fidelity. For the chosen parameters ($t = t_d$ and $\alpha = 1$), the dressed basis yields a higher fidelity than the bare basis. Additionally, the coupling strength has a larger impact on fidelity in the bare basis compared to the dressed basis.

Our numerical simulations reveal that, for small α , the bare basis yields higher fidelity compared to the dressed basis. However, the bare basis is more sensitive to the coupling strength between the flux qubits, demonstrating a significant decline in measurement quality as the coupling strength increases. Conversely, for large α , the dressed basis offers higher fidelity, characterized by oscillations with J . Notably, the average fidelity across these oscillations exhibits only a slight decrease, suggesting that these may be transient oscillations. This transient nature is possibly due to the non-adiabatic change in the operating point and the presence of multiple energy levels in the system.

2. Energy basis of both flux qubits

This section analyzes the Hamiltonian operator in the q_1 - q_2 energy basis (Eq. (39)). Due to its complexity, we adopt an analytical approach by focusing on two specific interaction regimes between two flux qubits: flux-dominated and tunneling-dominated regimes.

Within the regime defined by

$$\{|\cos(\theta_1)|, |\cos(\theta_{\text{eff},2})|\} \gg \{|\sin(\theta_1)|, |\sin(\theta_{\text{eff},2})|\}, \quad (49)$$

we can approximate the interaction term between q_1 and q_2 as $J_{zz}\hat{\sigma}_1^z\hat{\sigma}_2^z$ with $J_{zz} = J \cos(\theta_1) \cos(\theta_{\text{eff},2})$, leading to

$$\hat{H}_{zz}^{(e)} \approx -\frac{\hat{\delta}_{\text{eff}2,n}}{2}\hat{\sigma}_2^z + J_{zz}\hat{\sigma}_1^z\hat{\sigma}_2^z. \quad (50)$$

We refer to this approximation as the zz approximation. Under this approximation, $\tilde{H}_{zz}^{(3)}$ becomes a diagonal matrix, implying that the q_1 - q_2 energy basis already coincides with the dressed basis. Consequently, the criterion for a valid RWA is automatically fulfilled. This signifies that the zz approximation inherently guarantees higher fidelity.

Figure 7 shows the fidelity in the q_1 - q_2 energy basis and the fidelity with the Hamiltonian under zz approxi-

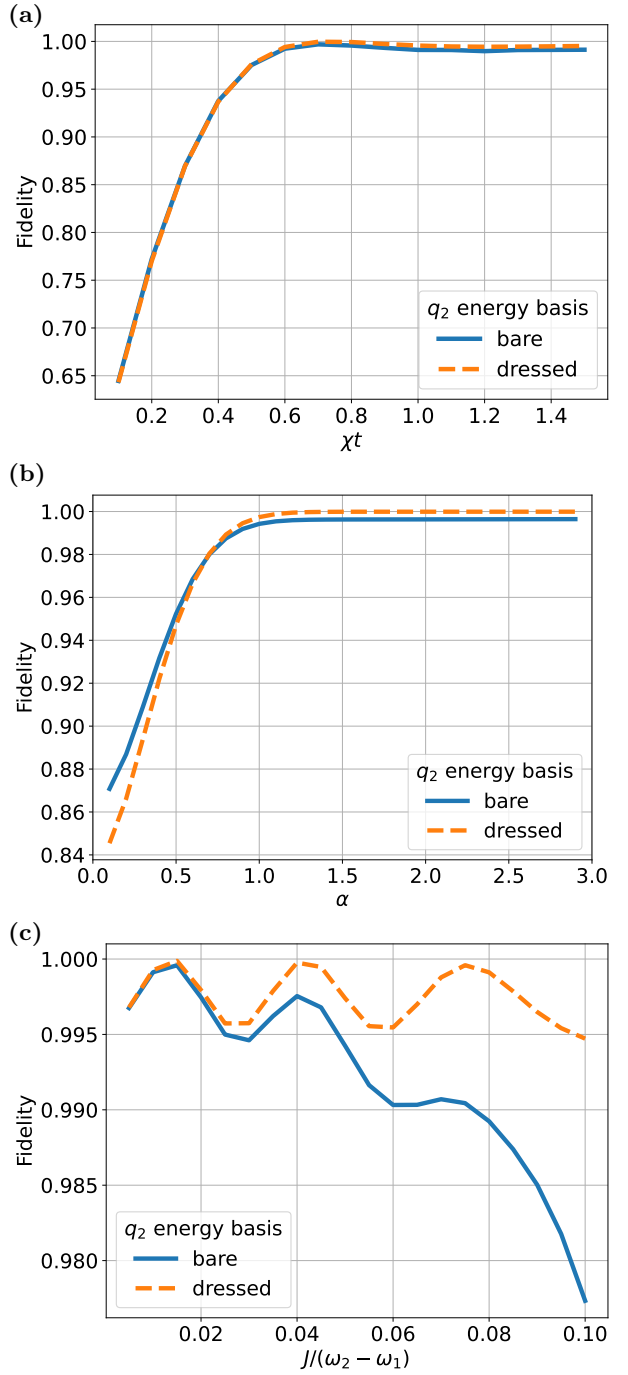


FIG. 6. Fidelity in bare and dressed bases calculated using the Hamiltonian expressed in the q_2 energy basis. Parameters are the same as in Fig. 5.

mation. In the q_1 - q_2 energy basis, fidelity increases monotonically with χt and saturates at a certain value. Under zz approximation, fidelity damped oscillates around the value in q_1 - q_2 energy basis (Fig. 7(a)). This oscillation in the zz approximation allows for high fidelity even at shorter measurement times. Additionally, both bases achieve the highest fidelity at a measurement time

of $t \approx t_d$. As shown in Fig. 7(b), the fidelity under zz approximation is consistently higher for all values of α , with the difference being more pronounced for smaller values. When α exceeds 1, both bases exhibit almost identical fidelity. Figure 7(c) demonstrates that under zz approximation, fidelity oscillates around 0.998 with increasing $J/(\omega_2 - \omega_1)$. In contrast, the q_1 - q_2 energy basis exhibits a decreasing trend with increasing coupling strength, and the fidelity is also lower for smaller values of J . Both bases show transient oscillations, probably due to the non-adiabatic change in the operating point and the presence of multiple energy levels. The results demonstrate that the zz approximation consistently achieves higher fidelity than the original q_1 - q_2 energy basis, suggesting that incorporating the flux dominant regime could be beneficial for achieving high fidelity qubit readout.

We now explore the tunneling-dominated regime, characterized by

$$\{|\cos(\theta_1)|, |\cos(\theta_{\text{eff},2})|\} \ll \{|\sin(\theta_1)|, |\sin(\theta_{\text{eff},2})|\}. \quad (51)$$

In this regime, the interaction between flux qubits simplifies to the xx approximation $J_{xx}\hat{\sigma}_1^x\hat{\sigma}_2^x$ with $J_{xx} = J \sin(\theta_1) \sin(\theta_{\text{eff},2})$, resulting in the Hamiltonian

$$\hat{H}_{xx}^{(e)} \approx -\frac{\hat{\delta}_{\text{eff}2,n}}{2}\tilde{\sigma}_2^z + J_{xx}\tilde{\sigma}_1^x\tilde{\sigma}_2^x. \quad (52)$$

Diagonalizing $\hat{H}_{xx}^{(e)}$, we obtain eigenstates

$$\begin{aligned} |\overline{00}\rangle &= \cos\left(\frac{\theta_{0+}}{2}\right)|\tilde{0}\tilde{0}\rangle + \sin\left(\frac{\theta_{0+}}{2}\right)|\tilde{1}\tilde{1}\rangle, \\ |\overline{01}\rangle &= \cos\left(\frac{\theta_{0-}}{2}\right)|\tilde{0}\tilde{1}\rangle + \sin\left(\frac{\theta_{0-}}{2}\right)|\tilde{1}\tilde{0}\rangle, \\ |\overline{10}\rangle &= -\sin\left(\frac{\theta_{0-}}{2}\right)|\tilde{0}\tilde{1}\rangle + \cos\left(\frac{\theta_{0-}}{2}\right)|\tilde{1}\tilde{0}\rangle, \\ |\overline{11}\rangle &= -\sin\left(\frac{\theta_{0+}}{2}\right)|\tilde{0}\tilde{0}\rangle + \cos\left(\frac{\theta_{0+}}{2}\right)|\tilde{1}\tilde{1}\rangle, \end{aligned} \quad (53)$$

where $\theta_{n\pm}$ is defined as $\tan(\theta_{n\pm}) = \pm 2J_{xx}/\delta_{\text{eff}2,n}$. The corresponding eigenvalues are

$$E_{xx}^{(e)} = \{-\omega_n, -\omega_n, \omega_n, \omega_n\}, \quad (54)$$

where $\omega_n = \sqrt{J_{xx}^2 + (\delta_{\text{eff}2,n}/2)^2}$. This allows us to represent the Hamiltonian in the dressed basis

$$\begin{aligned} \bar{H}_{xx}^{(e)} = \frac{\omega_n}{2} & [\cos(\theta_{n-} - \theta_{0-}) (\bar{\sigma}_1^z + \bar{\sigma}_2^z) \\ & + \sin(\theta_{n-} - \theta_{0-}) (\bar{\sigma}_1^x\bar{\sigma}_2^x - \bar{\sigma}_1^y\bar{\sigma}_2^y) \\ & + \cos(\theta_{n+} - \theta_{0+}) (\bar{\sigma}_1^z - \bar{\sigma}_2^z) \\ & + \sin(\theta_{n+} - \theta_{0+}) (\bar{\sigma}_1^x\bar{\sigma}_2^x + \bar{\sigma}_1^y\bar{\sigma}_2^y)]. \end{aligned} \quad (55)$$

The valid RWA condition for dressed basis is given by

$$\left\| \frac{J_{xx} \chi (\hat{a}^\dagger \hat{a} + \frac{1}{2})}{\hat{\delta}_{\text{eff}2,n} \delta_{\text{eff}2,n}/4 + J_{xx}^2} \right\| \ll 1. \quad (56)$$

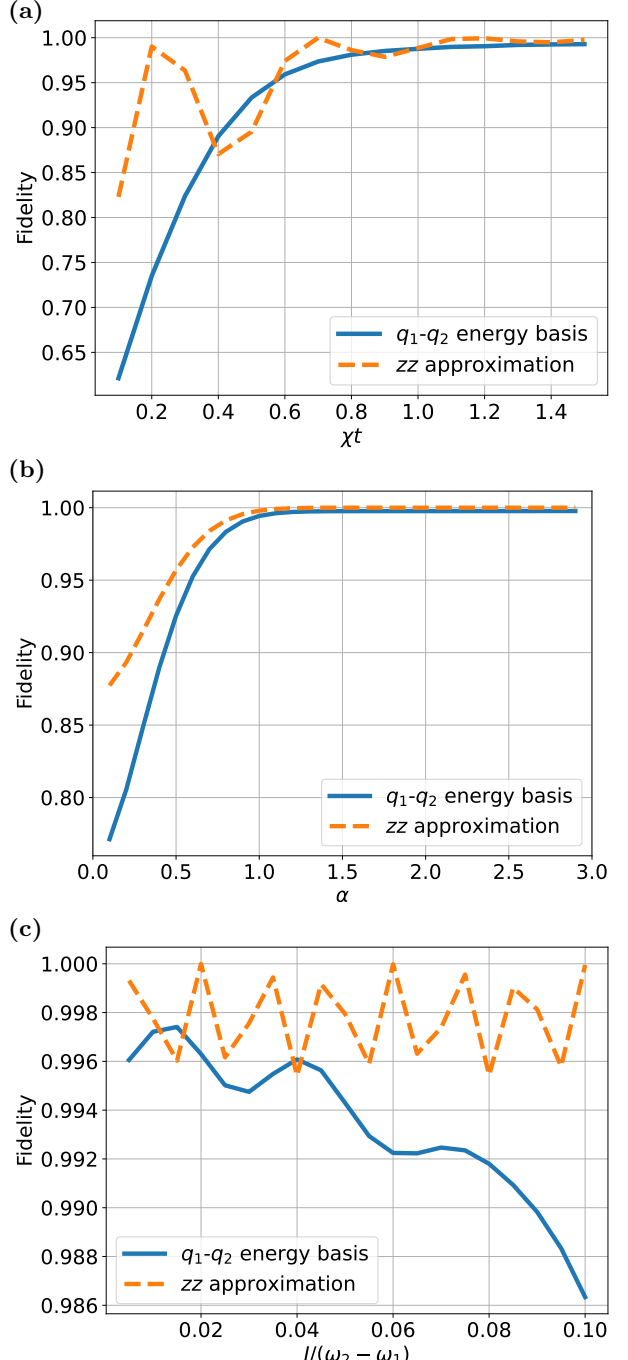


FIG. 7. Fidelity calculated using the Hamiltonian expressed in the q_1 - q_2 energy basis without approximation and under the zz approximation. Parameters are the same as in Fig. 5.

In comparison, the valid RWA condition for the bare basis is

$$\left\| \frac{J_{xx}}{\hat{\delta}_{\text{eff}2,n}/2} \right\| \ll 1. \quad (57)$$

If the condition

$$\left\| \chi \left(\hat{a}^\dagger \hat{a} + \frac{1}{2} \right) \right\| = \sqrt{(\delta_{\text{eff},2}/2)^2 + J_{xx}^2} \quad (58)$$

is satisfied, there is no distinction between bare and dressed bases. Consequently, this provides the criterion for a basis crossover in the q_1 - q_2 energy basis representation in the tunneling-dominated regime.

Figure 8 presents results of a numerical investigation of fidelity using a Hamiltonian under xx approximation, comparing bare and dressed bases. As shown in Fig. 8(a), maximum fidelity is achieved in both bases around a measurement time of $t \approx t_d$. However, for $t > t_d/\pi$, the dressed basis surpasses the bare basis. A similar trend is observed in Fig. 8(b). When the amplitude of the resonator coherent state is relatively small, $\alpha \lesssim 0.5$, the fidelity in both bases shows minimal difference. As α increases, the dressed basis exhibits both higher fidelity and saturation value. Figure 8(c) demonstrates that increasing the coupling strength negatively impacts the fidelity in the bare basis. Conversely, fidelity in a dressed basis remains consistently high, demonstrating robustness against changes in coupling strength. The results highlight the advantage of a dressed basis over a bare basis. Specifically, while the bare basis exhibits high sensitivity to changes in coupling strength, the dressed basis exhibits remarkable resilience to such perturbations and maintains a consistently high fidelity.

To summarize, we have investigated the condition for a valid RWA within the q_1 - q_2 energy basis by analyzing two scenarios, including zz and xx approximations. Under the zz approximation, the Hamiltonian already exists in a diagonalized form, automatically satisfying the RWA condition. This simplifies analysis and guarantees higher fidelity. In contrast, the xx approximation necessitates a specific condition for a valid RWA. Employing a dressed basis offers potential advantages in terms of fidelity and robustness.

B. Simultaneous measurement

This section explores the simultaneous measurement model, in which both QFP₁ and QFP₂ undergo adiabatic annealing, as shown in Fig. 9. Then, the state of QFP₂ is measured using a resonator. In contrast to the sequential model, where one qubit is actively measured while the other is assumed to be static, the simultaneous measurement model keeps both qubits dynamically involved. After annealing, the states of flux qubits q_1 and q_2 are latched into their respective QFP₁ and QFP₂. The primary focus is on reading out the state of QFP₂ via its associated resonator, while any interaction of QFP₁ with a potentially connected resonator is neglected. This simplification is valid because once latched, QFP₁'s state no longer influences QFP₂ or the resonator connected to QFP₂. To ensure this isolation, we assume negligible interactions between QFPs, achieved through an optimized

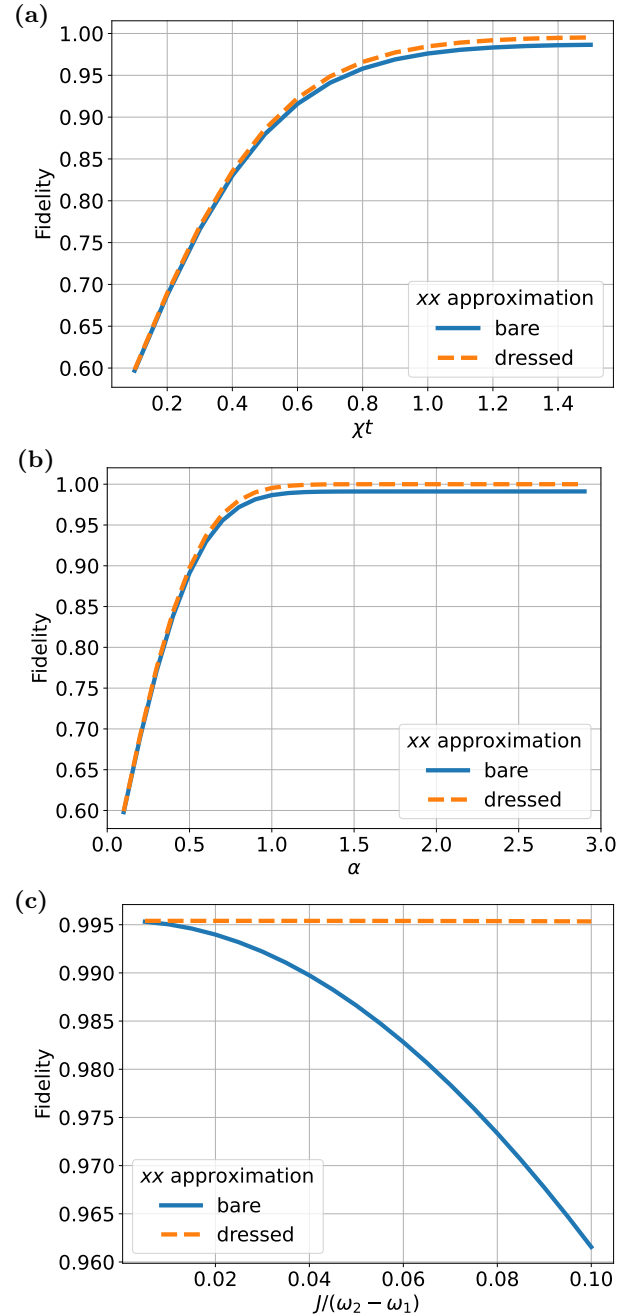


FIG. 8. Fidelity in bare and dressed bases calculated using the Hamiltonian expressed in the q_1 - q_2 energy basis under the xx approximation with $N = 27$, $\eta = 1.25$, $\Delta_2/\epsilon_2 = 10$, and $\delta/g = 8$. Parameters are: (a) $J/(\omega_2 - \omega_1) = 0.05$ and $\alpha = 1$; (b) $J/(\omega_2 - \omega_1) = 0.05$ and $t = t_d$; and (c) $t = t_d$ and $\alpha = 1$.

design featuring sufficient spatial separation, minimized mutual inductance, and distinct operational frequencies to effectively suppress crosstalk. Consequently, the system is characterized by a Hamiltonian expressed in the

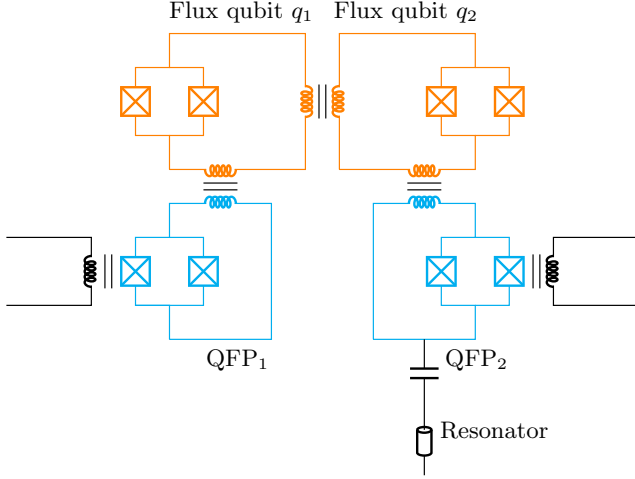


FIG. 9. Simultaneous measurement model. Each flux qubit signal is coupled with a QFP. Through adiabatic annealing, the flux qubit state is latched into the corresponding QFP. Then, QFP₂ is read out using a resonator.

flux basis

$$\hat{H} = -\frac{1}{2}(\epsilon_1 \hat{\sigma}_1^z + \Delta_{\text{eff},1} \hat{\sigma}_1^x) - \frac{1}{2}(\epsilon_2 \hat{\sigma}_2^z + \Delta_{\text{eff},2} \hat{\sigma}_2^x) + J \hat{\sigma}_1^z \hat{\sigma}_2^z + g_2 \hat{\sigma}_2^z (\hat{a}^\dagger + \hat{a}) + \omega_r \hat{a}^\dagger \hat{a}, \quad (59)$$

where ϵ_1 and ϵ_2 are energies of q_1 and q_2 , respectively, $\Delta_{\text{eff},1}$ and $\Delta_{\text{eff},2}$ are the corresponding effective detunings, ω_r is resonator frequency, J denotes coupling strength between two flux qubits, and g_2 corresponds to coupling strength between QFP₂ and resonator.

In q_1 - q_2 energy basis, the Hamiltonian becomes

$$\begin{aligned} \tilde{H} = & -\frac{\omega_{\text{eff},1}}{2} \tilde{\sigma}_1^z + g_2 [\cos(\theta_{\text{eff},2}) \tilde{\sigma}_2^z - \sin(\theta_{\text{eff},2}) \tilde{\sigma}_2^x] (\hat{a}^\dagger + \hat{a}) \\ & -\frac{\omega_{\text{eff},2}}{2} \tilde{\sigma}_2^z + \omega_r \hat{a}^\dagger \hat{a} + J [\cos(\theta_{\text{eff},1}) \tilde{\sigma}_1^z - \sin(\theta_{\text{eff},1}) \tilde{\sigma}_1^x] \\ & \otimes [\cos(\theta_{\text{eff},2}) \tilde{\sigma}_2^z - \sin(\theta_{\text{eff},2}) \tilde{\sigma}_2^x], \end{aligned} \quad (60)$$

where $\omega_{\text{eff},i} = \sqrt{\epsilon_i^2 + \Delta_{\text{eff},i}^2}$ and $\theta_{\text{eff},i}$ is defined as $\tan(\theta_{\text{eff},i}) = \Delta_{\text{eff},i}/\epsilon_i$ with $i \in \{1, 2\}$. Applying the displacement operator $\hat{D}(\alpha)$ with $\alpha = -g_2 \cos(\theta_{\text{eff},2}) \tilde{\sigma}_2^z / \omega_r$, we obtain the Hamiltonian under the RWA

$$\begin{aligned} \tilde{H} = & -\frac{\omega_{\text{eff},1}}{2} \tilde{\sigma}_1^z - g_2 \sin(\theta_{\text{eff},2}) (\hat{a}^\dagger \tilde{\sigma}_2^- + \hat{a} \tilde{\sigma}_2^+) + \omega_r \hat{a}^\dagger \hat{a} \\ & -\frac{\omega_{\text{eff},2}}{2} \tilde{\sigma}_2^z + J [\cos(\theta_{\text{eff},1}) \tilde{\sigma}_1^z - \sin(\theta_{\text{eff},1}) \tilde{\sigma}_1^x] \\ & \otimes [\cos(\theta_{\text{eff},2}) \tilde{\sigma}_2^z - \sin(\theta_{\text{eff},2}) \tilde{\sigma}_2^x]. \end{aligned} \quad (61)$$

Further eliminating the interaction term between qubit and resonator by applying the unitary operator $\hat{U} = \exp[\lambda_2 (\hat{a} \tilde{\sigma}_2^+ - \hat{a}^\dagger \tilde{\sigma}_2^-)]$ with $\lambda_2 = g_2 \sin(\theta_{\text{eff},2}) / \Delta_{\text{eff},2}$,

we obtain

$$\begin{aligned} \hat{H} = & -\frac{\omega_{\text{eff},1}}{2} \tilde{\sigma}_1^z - \left(\frac{\omega_{\text{eff},2} + \chi}{2} + \chi \hat{a}^\dagger \hat{a} \right) \tilde{\sigma}_2^z + \omega_r \hat{a}^\dagger \hat{a} \\ & + J [\cos(\theta_{\text{eff},1}) \tilde{\sigma}_1^z - \sin(\theta_{\text{eff},1}) \tilde{\sigma}_1^x] \\ & \otimes [\cos(\theta_{\text{eff},2}) \tilde{\sigma}_2^z - \sin(\theta_{\text{eff},2}) \tilde{\sigma}_2^x]. \end{aligned} \quad (62)$$

Finally, transforming to a frame rotating at the frequency of ω_r , the Hamiltonian becomes

$$\begin{aligned} \tilde{H}_{(e)} = & -\frac{\delta_{\text{eff},1}}{2} \tilde{\sigma}_1^z - \frac{\hat{\delta}_{\text{eff},2,n}}{2} \tilde{\sigma}_2^z + J [\cos(\theta_{\text{eff},1}) \tilde{\sigma}_1^z - \sin(\theta_{\text{eff},1}) \tilde{\sigma}_1^x] [\cos(\theta_{\text{eff},2}) \tilde{\sigma}_2^z - \sin(\theta_{\text{eff},2}) \tilde{\sigma}_2^x], \end{aligned} \quad (63)$$

where $\delta_{\text{eff},i} = \omega_{\text{eff},i} - \omega_r$ with $i \in \{1, 2\}$, and $\hat{\delta}_{\text{eff},2,n} = \delta_{\text{eff},2} + \chi(2\hat{n} + 1)$ with $\hat{n} = \hat{a}^\dagger \hat{a}$ and $\chi = g_2^2 \sin^2(\theta_{\text{eff},2}) / \Delta_{\text{eff},2}$. Transforming back into the flux basis yields

$$\begin{aligned} \hat{H}_{(f)} = & -\frac{\delta_{\text{eff},1}}{2} [\cos(\theta_{\text{eff},1}) \hat{\sigma}_1^z + \sin(\theta_{\text{eff},1}) \hat{\sigma}_1^x] + J \hat{\sigma}_1^z \hat{\sigma}_2^z \\ & -\frac{\hat{\delta}_{\text{eff},2,n}}{2} [\cos(\theta_{\text{eff},2}) \hat{\sigma}_2^z + \sin(\theta_{\text{eff},2}) \hat{\sigma}_2^x]. \end{aligned} \quad (64)$$

Similar to the previous analysis, we consider flux-dominated and tunneling-dominated regimes.

1. Flux-dominated regime

We first analyze the Hamiltonian within the flux-dominated regime, assuming

$$\{|\cos(\theta_{\text{eff},1})|, |\cos(\theta_{\text{eff},2})|\} \gg \{|\sin(\theta_{\text{eff},1})|, |\sin(\theta_{\text{eff},2})|\}. \quad (65)$$

Under this condition, the interaction between q_1 and q_2 can be approximated as $J_{zz} \tilde{\sigma}_1^z \tilde{\sigma}_2^z$ with $J_{zz} = J \cos(\theta_{\text{eff},1}) \cos(\theta_{\text{eff},2})$, referring to as zz approximation. This approximation leads to a simplified Hamiltonian

$$\tilde{H}_{zz}^{(3)} \approx -\frac{\delta_{\text{eff},1}}{2} \tilde{\sigma}_1^z - \frac{\hat{\delta}_{\text{eff},2,n}}{2} \tilde{\sigma}_2^z + J_{zz} \tilde{\sigma}_1^z \tilde{\sigma}_2^z. \quad (66)$$

Figure 10 presents simulation results comparing the fidelity of measuring q_2 using a simultaneous measurement model in three cases: Hamiltonian expressed in flux basis, Hamiltonian expressed in q_1 - q_2 energy basis, and Hamiltonian expressed in q_1 - q_2 energy basis under zz approximation. Figure 10(a) shows that high fidelity can be achieved with short measurement times, potentially due to the diagonalized term $J \hat{\sigma}_1^z \hat{\sigma}_2^z$ in Hamiltonian (Eq. (64)), which plays a crucial role in satisfying the RWA conditions. Figure 10(b) indicates that under the zz approximation, fidelity increases with α until reaching a saturation value. While the fidelity in flux and q_1 - q_2 energy bases is higher than under zz approximation for $\alpha \lesssim 0.4$, it decreases before reaching a maximum at

$\alpha \approx 3.3$, ultimately settling below zz approximation fidelity. At large values of α , fidelity decreases slightly in all cases, possibly due to the breakdown of the approximation for $\alpha^2 \ll N$. As shown in Fig. 10(c), when coupling strengths are weak ($J/(\omega_2 - \omega_1) \lesssim 0.005$), all cases exhibit comparable fidelity. However, the zz approximation generally achieves higher overall fidelity, which is possibly due to the choice of optimal measurement time ($t = t_d/2$) (see Fig. 10(a)). While the coupling between flux qubits is crucial in this model compared to the previous one, leading to different system dynamics, flux basis and q_1 - q_2 energy basis exhibit similar trends.

2. Tunneling-dominated regime

This section explores the tunneling-dominated regime under the condition

$$\{|\cos(\theta_{\text{eff},1})|, |\cos(\theta_{\text{eff},2})|\} \ll \{|\sin(\theta_{\text{eff},1})|, |\sin(\theta_{\text{eff},2})|\}. \quad (67)$$

Within this regime, we approximate the interaction term between q_1 and q_2 as $J_{xx}\hat{\sigma}_1^x\hat{\sigma}_2^x$ (the xx approximation), where $J_{xx} = J \sin(\theta_{\text{eff},1}) \sin(\theta_{\text{eff},2})$, leading to the simplified Hamiltonian

$$\tilde{H}_{xx}^{(3)} = -\frac{\delta_{\text{eff},1}}{2}\tilde{\sigma}_1^z - \frac{\hat{\delta}_{\text{eff}2,n}}{2}\tilde{\sigma}_2^z + J_{xx}\tilde{\sigma}_1^x\tilde{\sigma}_2^x. \quad (68)$$

Analogously, we obtain the condition for good RWA in the dressed basis through the diagonalization of the Hamiltonian

$$\left\| \frac{J_{xx} \left[(\delta_{\text{eff},2} \pm \delta_{\text{eff},1}) \pm (\hat{\delta}_{\text{eff}2,n} \pm \delta_{\text{eff},1}) \right] / 2}{(\delta_{\text{eff},2} \pm \delta_{\text{eff},1})(\hat{\delta}_{\text{eff}2,n} \pm \delta_{\text{eff},1}) / 4 + J_{xx}^2} \right\| \ll 1, \quad (69)$$

where $\theta_{n\pm}$ is defined as $\tan(\theta_{n\pm}) = 2J_{xx} / (\delta_{\text{eff}2,n} \pm \delta_{\text{eff},1})$. In the bare basis, the condition becomes

$$\left\| \frac{J_{xx}}{(\hat{\delta}_{\text{eff}2,n} \pm \delta_{\text{eff},1}) / 2} \right\| \ll 1. \quad (70)$$

The equation for the crossover point between bare and dressed bases is given by

$$\left\| \chi \left(\hat{a}^\dagger \hat{a} + \frac{1}{2} \right) \right\| = \sqrt{(\delta_{\text{eff},2} - \delta_{\text{eff},1})^2 / 4 + J_{xx}^2}. \quad (71)$$

Figure 11 presents numerical results for fidelity in the tunneling-dominated regime. As shown in Fig. 11(a), at a short measurement time ($t \approx 0.06t_d$), the bare basis exhibits significantly higher fidelity, while at a long measurement time ($t \approx t_d$), the dressed basis performs better. This demonstrates the possibility of achieving high fidelity in a bare basis with short measurements. For small values of α , the bare basis exhibits higher fidelity, as depicted in Fig. 11(b). In a dressed basis, fidelity

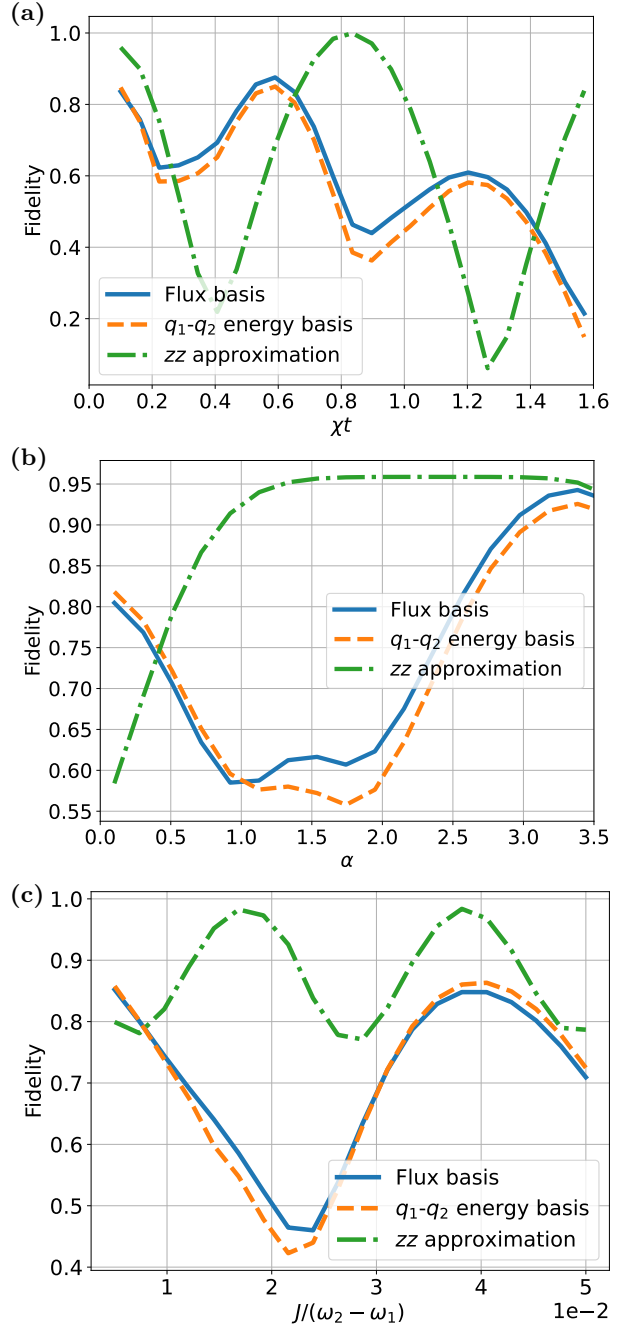


FIG. 10. Fidelity calculated using the Hamiltonian expressed in the flux basis, the q_1 - q_2 energy basis without approximation, and under the zz approximation with $N = 21$, $\eta = 1.25$, $\Delta_2/\epsilon_2 = 0.5$, and $\delta/g = 8$. Parameters are: (a) $J/(\omega_2 - \omega_1) = 0.05$ and $\alpha = 2$; (b) $J/(\omega_2 - \omega_1) = 0.05$ and $t = t_d/2$; and (c) $t = t_d/2$ and $\alpha = 1$.

increases with rising α until reaching a maximum. However, when α exceeds a certain threshold, the condition $\alpha^2 \ll N$ is no longer met, leading to a decrease in fidelity. Notably, the bare basis seems more sensitive to changes in α compared to the dressed basis. Figure 11(c) shows the dependence of fidelity on the coupling strength be-

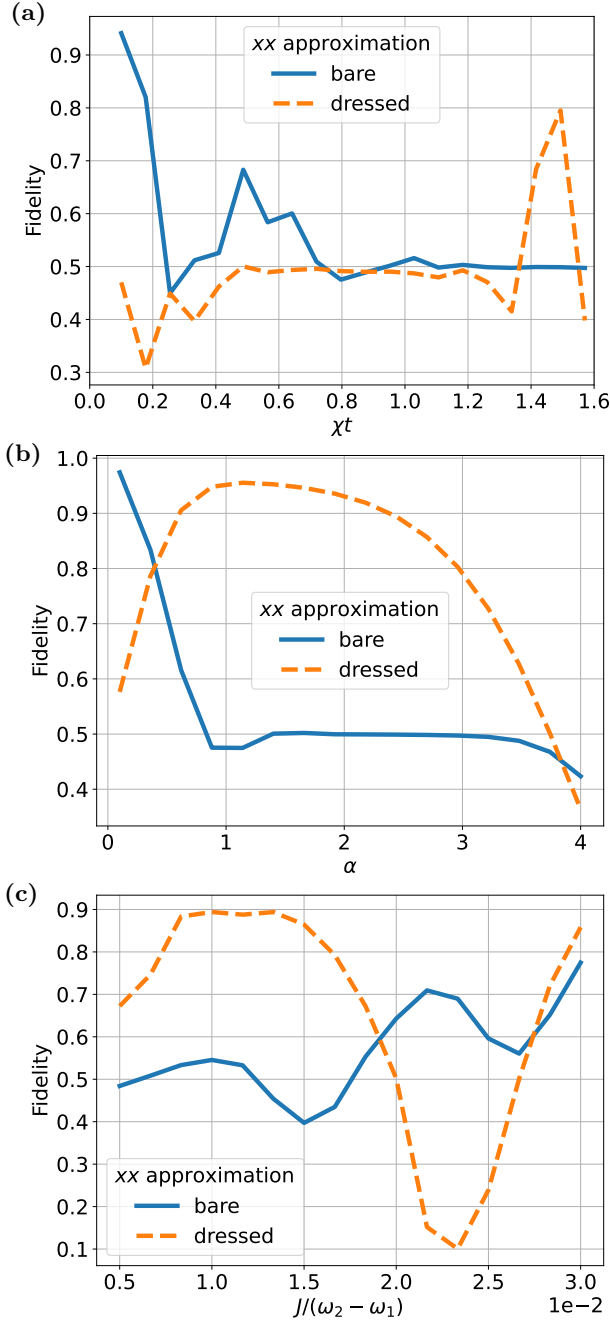


FIG. 11. Fidelity in bare and dressed bases calculated using the Hamiltonian expressed in the q_1 - q_2 energy basis under the xx approximation with $N = 21$, $\eta = 1$, $\Delta_2/\epsilon_2 = 8$, and $\delta/g = 8$. Parameters are: (a) $J/(\omega_2 - \omega_1) = 0.05$ and $\alpha = 2$; (b) $J/(\omega_2 - \omega_1) = 0.05$ and $t = t_d$; and (c) $t = t_d$ and $\alpha = 0.5$.

tween flux qubits. We observe that the fidelity oscillates in both bare and dressed bases, with the dressed basis exhibiting a stronger response to the interaction strength $J/(\omega_2 - \omega_1)$. A basis crossover is clearly illustrated between bare and dressed bases as the interaction strength changes.

The xx approximation leads to a distinct basis crossover driven by the interaction between flux qubits.

For short measurement times, bare basis offers an advantage, while dressed basis performs better at longer times. In addition, high fidelity can be achieved in both bare and dressed bases, depending on the value of α (small for bare and large for dressed). In contrast to previous models, the interaction between flux qubits has a stronger influence on the fidelity in the dressed basis here.

V. DISCUSSION AND CONCLUSIONS

We perform a systematic theoretical and numerical investigation of QFP-mediated measurements of flux qubits, focusing on the interplay between readout fidelity, measurement basis, and system parameters, such as measurement time, resonator coherent state amplitude, and qubit-qubit coupling strength. Using the QFP as an intermediary to latch and map the qubit state to a measurable quantity in the resonator, our approach provides a versatile framework for optimizing fidelity. This work offers two significant contributions: (i) a comprehensive comparison between energy and flux bases for readouts, demonstrating that the energy basis often yields higher fidelity in a wide range of scenarios, and (ii) an in-depth analysis of how QFP annealing processes affect fidelity and the selection of optimal readout strategies.

Our results highlight the QFP's ability to enable high-fidelity readout via adiabatic annealing, effectively latching the qubit state and enabling an effective flux qubit Hamiltonian description after annealing. We show that this process establishes entanglement between the qubit and QFP in both flux and energy bases, providing a robust means of transferring the state information into a form amenable to dispersive readout. Critically, our comparison of single-qubit readouts in different bases supports theoretical predictions that the energy basis generally outperforms the flux basis, underscoring the importance of basis selection for practical quantum readout protocols.

Extending beyond the single-qubit scenario, we examine the measurement of a target qubit in a two-qubit system. We investigate two distinct measurement models: sequential and simultaneous measurements. These analyses demonstrate the influence of the QFP annealing sequence on measurement fidelity. Sequential measurement consistently achieves high fidelity in energy bases and demonstrates greater resilience to qubit coupling than flux bases. However, this robustness is offset by slower measurement times, as fidelity degrades at very short measurement durations. Conversely, the simultaneous readout model utilizes QFP annealing for both qubits, enabling high fidelity at shorter timescales and offering a pathway to rapid and efficient measurements. Nonetheless, the added complexity of annealing sequences in the simultaneous scheme presents potential practical challenges. These findings provide a guiding framework for the design of scalable, high-fidelity readout architectures in multi-qubit circuits.

Future research will focus on extending these analyses to open quantum systems and incorporating realistic noise and decoherence models. This will be essential to bridge the gap between idealized theoretical predictions and the performance of real superconducting qubit devices. Further investigation into the origin and suppression of oscillatory dynamics in coupled qubit systems could lead to further improvements in readout fidelity. Finally, scaling these approaches to larger qubit networks and more intricate QFP-based architectures promises to establish fundamental principles for readout optimization in increasingly complex quantum processors. By advancing the integration of system design, basis selection, and measurement strategy, we aim to contribute to the development of robust, high-fidelity qubit readouts, an indispensable step toward realizing practical fault-tolerant quantum computation.

ACKNOWLEDGMENTS

The authors would like to thank Uwe Hartmann and Marius Schöndorf for their useful discussions.

Appendix A: Backaction of QFP annealing on flux qubits

This section investigates the backaction effects of QFP annealing on flux qubits. We focus on deriving the effective Hamiltonian (Eq. (25)) that governs the coupled system of the flux qubit and QFP after the annealing process. Additionally, we analyze how QFP annealing affects the state of the flux qubit connected to the QFP and the coupling strength J (Eqs. (34) and (59)) between coupled flux qubits.

1. Effective Hamiltonian of the coupled flux qubit and QFP system

We begin by examining the Hamiltonian that describes the QFP and its interaction with the flux qubit, as given in Eq. (19)

$$\hat{H}_{\text{qfp}} = \tilde{\Omega}\hat{a}^\dagger\hat{a} + \tilde{g}\varphi_p(\hat{a}^\dagger + \hat{a})\hat{\sigma}_z. \quad (\text{A1})$$

By setting $\hat{\sigma}_z$ to its eigenvalues ± 1 , corresponding to the eigenstates $|0\rangle$ and $|1\rangle$, and considering the QFP eigenstates and eigenvalues of $|\phi_{\pm}\rangle$ and E , respectively, we obtain

$$\left[\tilde{\Omega}\hat{a}^\dagger\hat{a} \pm \tilde{g}\varphi_p(\hat{a}^\dagger + \hat{a})\right]|\phi_{\pm}\rangle = E|\phi_{\pm}\rangle. \quad (\text{A2})$$

Eq. (A2) can be rewritten as

$$\left(\hat{a}^\dagger \pm \frac{\tilde{g}\varphi_p}{\tilde{\Omega}}\right)\left(\hat{a} \pm \frac{\tilde{g}\varphi_p}{\tilde{\Omega}}\right)|\phi_{\pm}\rangle = \left(\frac{E}{\tilde{\Omega}} + \frac{\tilde{g}^2\varphi_p^2}{\tilde{\Omega}^2}\right)|\phi_{\pm}\rangle. \quad (\text{A3})$$

Assuming $\frac{\tilde{g}\varphi_p}{\tilde{\Omega}}$ is real, the left-hand side of Eq. (A3) becomes

$$\left(\hat{a}^\dagger \pm \frac{\tilde{g}\varphi_p}{\tilde{\Omega}}\right)\left(\hat{a} \pm \frac{\tilde{g}\varphi_p}{\tilde{\Omega}}\right)|\phi_{\pm}\rangle = \hat{D}\left(\mp\frac{\tilde{g}\varphi_p}{\tilde{\Omega}}\right)\hat{a}^\dagger\hat{a}\hat{D}^\dagger\left(\mp\frac{\tilde{g}\varphi_p}{\tilde{\Omega}}\right), \quad (\text{A4})$$

where $\hat{D}(\nu) = \exp\{\nu(\hat{a}^\dagger - \hat{a})\}$ is the displacement operator. Consequently, the eigenstates are expressed as

$$|\phi_{\pm}\rangle = \hat{D}\left(\mp\frac{\tilde{g}\varphi_p}{\tilde{\Omega}}\right)|M\rangle \equiv |M_{\pm}\rangle, \quad (\text{A5})$$

where $|M\rangle$ are Fock states for $M = 0, 1, 2, \dots$. The corresponding eigenvalues are

$$E_M = \tilde{\Omega}\left(M - \frac{\tilde{g}^2\varphi_p^2}{\tilde{\Omega}^2}\right). \quad (\text{A6})$$

The Hamiltonian \hat{H}_{qfp} (Eq. (A1)) can then be diagonalized by applying the displacement operator

$$\tilde{\hat{H}}_{\text{qfp}} = \hat{D}^\dagger(\mp\tilde{g}\varphi_p)\hat{H}_{\text{qfp}}\hat{D}(\mp\tilde{g}\varphi_p) = \tilde{\Omega}\hat{a}^\dagger\hat{a}. \quad (\text{A7})$$

This transformation also affects the flux qubit Hamiltonian \hat{H}_q , given by

$$\hat{H}_q = -\frac{1}{2}(\epsilon_q\hat{\sigma}_z + \Delta_q\hat{\sigma}_x), \quad (\text{A8})$$

leading to

$$\begin{aligned} \tilde{\hat{H}}_q &= \hat{D}^\dagger(\mp\tilde{g}\varphi_p)\hat{H}_q\hat{D}(\mp\tilde{g}\varphi_p) \\ &= \hat{D}(\pm\tilde{g}\varphi_p)\hat{H}_q\hat{D}^\dagger(\pm\tilde{g}\varphi_p) \\ &= \hat{D}(\hat{\sigma}_z\tilde{g}\varphi_p)\hat{H}_q\hat{D}^\dagger(\hat{\sigma}_z\tilde{g}\varphi_p). \end{aligned} \quad (\text{A9})$$

Leveraging the following relations

$$\hat{D}(\hat{\sigma}_z\tilde{g}\varphi_p)\hat{\sigma}_z\hat{D}^\dagger(\hat{\sigma}_z\tilde{g}\varphi_p) = \hat{\sigma}_z, \quad (\text{A10})$$

$$\hat{D}(\hat{\sigma}_z\tilde{g}\varphi_p)\hat{\sigma}_x\hat{D}^\dagger(\hat{\sigma}_z\tilde{g}\varphi_p) = \hat{\sigma}_x + 2\tilde{\Omega}\hat{p}\hat{\sigma}_y, \quad (\text{A11})$$

where $\hat{p} = i\sqrt{m\Omega/2}(\hat{a}^\dagger - \hat{a}) = m\frac{d\varphi_p}{dt}$, the term \hat{p} is assumed to be negligible under adiabatic conditions and is excluded from subsequent calculations. Under this approximation, Eq. (19) simplifies to [10, 39]

$$\hat{H} = \bigoplus_{N=0}^{\infty} \hat{H}_M, \quad (\text{A12})$$

where \hat{H}_M is the Hamiltonian in the M -excitation subspace $\{|0, M_+\rangle, |1, M_-\rangle\}$ and is expressed as

$$\hat{H}_M = \begin{bmatrix} E_M - \epsilon/2 & -\Delta\langle M_- | M_+ \rangle / 2 \\ -\Delta\langle M_- | M_+ \rangle / 2 & E_M + \epsilon/2 \end{bmatrix}, \quad (\text{A13})$$

or equivalently

$$\hat{H}_M = E_M \mathbb{1} - \frac{\epsilon}{2}\hat{\sigma}_z - \frac{\Delta_{\text{eff}}}{2}\hat{\sigma}_x \quad (\text{A14})$$

with $\Delta_{\text{eff}} = \Delta \langle M_- | M_+ \rangle$. The overlap $\langle M_- | M_+ \rangle$ is given by [39]

$$\langle M_- | M_+ \rangle = e^{-\eta} L_M(2\eta), \quad (\text{A15})$$

where $\eta = 2\tilde{g}^2\varphi_p^2/\tilde{\Omega}^2 = m\Omega\varphi_p^2$ and L_M is the Laguerre polynomial. Assuming the harmonic oscillator is in its ground state ($M = 0$), the effective Hamiltonian in Eq. (25) is obtained by neglecting the constant term in Eq. (A14). In this case, Δ_{eff} is given by

$$\Delta_{\text{eff}} = \Delta \langle 0_- | 0_+ \rangle = \Delta e^{-\eta}. \quad (\text{A16})$$

2. Backaction of QFP annealing on coupled flux qubits

Here we demonstrate that the coupling strength J between two flux qubits in Eq. (34) remains unaffected during the QFP annealing process. The interaction Hamiltonian describing two coupled flux qubits is given by

$$\hat{H}_I = J\hat{\sigma}_1^z\hat{\sigma}_2^z. \quad (\text{A17})$$

Analogous to the analysis in Eq. A9, the backaction of QFP annealing can be evaluated by applying the displacement operator to \hat{H}_I

$$\hat{H}_I = \hat{D}(\hat{\sigma}_2^z\tilde{g}\varphi_p)\hat{H}_I\hat{D}^\dagger(\hat{\sigma}_2^z\tilde{g}\varphi_p). \quad (\text{A18})$$

Applying this transformation yields

$$\hat{H}_I = J\hat{\sigma}_1^z\hat{D}(\hat{\sigma}_2^z\tilde{g}\varphi_p)\hat{\sigma}_2^z\hat{D}^\dagger(\hat{\sigma}_2^z\tilde{g}\varphi_p), \quad (\text{A19})$$

$$= J\hat{\sigma}_1^z\hat{\sigma}_2^z = \hat{H}_I. \quad (\text{A20})$$

This result indicates that the interaction Hamiltonian \hat{H}_I remains unchanged after the transformation, implying that the coupling strength J between the two flux qubits is unaffected by the QFP annealing process.

Similarly, the coupling strength J in Eq. (59) is also not renormalized by the QFP annealing. The consistency of J before and after the annealing process ensures that the qubit-qubit interactions are preserved, which is crucial for maintaining the integrity of quantum operations in coupled qubit systems.

[1] J. Clarke and F. K. Wilhelm, Superconducting quantum bits, *Nature* **453**, 1031 (2008).

[2] P. Krantz, M. Kjaergaard, F. Yan, T. P. Orlando, S. Gustavsson, and W. D. Oliver, A quantum engineer's guide to superconducting qubits, *Applied physics reviews* **6** (2019).

[3] V. Bouchiat, D. Vion, P. Joyez, D. Esteve, and M. Devoret, Quantum coherence with a single cooper pair, *Physica Scripta* **1998**, 165 (1998).

[4] Y. Nakamura, C. D. Chen, and J. S. Tsai, Spectroscopy of energy-level splitting between two macroscopic quantum states of charge coherently superposed by josephson coupling, *Phys. Rev. Lett.* **79**, 2328 (1997).

[5] J. M. Martinis, Superconducting phase qubits, *Quantum information processing* **8**, 81 (2009).

[6] J. R. Friedman, V. Patel, W. Chen, S. Tolpygo, and J. E. Lukens, Quantum superposition of distinct macroscopic states, *Nature* **406**, 43 (2000).

[7] C. H. Van Der Wal, A. Ter Haar, F. Wilhelm, R. Schouten, C. Harmans, T. Orlando, S. Lloyd, and J. Mooij, Quantum superposition of macroscopic persistent-current states, *Science* **290**, 773 (2000).

[8] J. Koch, T. M. Yu, J. Gambetta, A. A. Houck, D. I. Schuster, J. Majer, A. Blais, M. H. Devoret, S. M. Girvin, and R. J. Schoelkopf, Charge-insensitive qubit design derived from the cooper pair box, *Phys. Rev. A* **76**, 042319 (2007).

[9] M. Stern, G. Catelani, Y. Kubo, C. Grezes, A. Bienfait, D. Vion, D. Esteve, and P. Bertet, Flux qubits with long coherence times for hybrid quantum circuits, *Phys. Rev. Lett.* **113**, 123601 (2014).

[10] M. Schöndorf, A. Lupaşcu, and F. K. Wilhelm, Flux-qubit readout in the persistent-current basis at arbitrary bias points, *Phys. Rev. A* **101**, 012305 (2020).

[11] R. Harris, J. Johansson, A. J. Berkley, M. W. Johnson, T. Lanting, S. Han, P. Bunyk, E. Ladizinsky, T. Oh, I. Perminov, E. Tolkacheva, S. Uchaikin, E. M. Chapple, C. Enderud, C. Rich, M. Thom, J. Wang, B. Wilson, and G. Rose, Experimental demonstration of a robust and scalable flux qubit, *Phys. Rev. B* **81**, 134510 (2010).

[12] J. Ferber and F. K. Wilhelm, Efficient creation of multipartite entanglement in flux qubits, *Nanotechnology* **21**, 274015 (2010).

[13] A. G. Fowler, W. F. Thompson, Z. Yan, A. M. Stephens, B. L. T. Plourde, and F. K. Wilhelm, Long-range coupling and scalable architecture for superconducting flux qubits, *Phys. Rev. B* **76**, 174507 (2007).

[14] T. L. Robertson, B. L. T. Plourde, T. Hime, S. Linzen, P. A. Reichardt, F. K. Wilhelm, and J. Clarke, Superconducting quantum interference device with frequency-dependent damping: Readout of flux qubits, *Phys. Rev. B* **72**, 024513 (2005).

[15] I. Chiorescu, Y. Nakamura, C. M. Harmans, and J. Mooij, Coherent quantum dynamics of a superconducting flux qubit, *Science* **299**, 1869 (2003).

[16] A. Blais, R.-S. Huang, A. Wallraff, S. M. Girvin, and R. J. Schoelkopf, Cavity quantum electrodynamics for superconducting electrical circuits: An architecture for quantum computation, *Phys. Rev. A* **69**, 062320 (2004).

[17] T. Walter, P. Kurpiers, S. Gasparinetti, P. Magnard, A. Potočnik, Y. Salathé, M. Pechal, M. Mondal, M. Oppliger, C. Eichler, and A. Wallraff, Rapid high-fidelity single-shot dispersive readout of superconducting qubits, *Phys. Rev. Appl.* **7**, 054020 (2017).

[18] J. Heinsoo, C. K. Andersen, A. Remm, S. Krinner, T. Walter, Y. Salathé, S. Gasparinetti, J.-C. Besse, A. Potočnik, A. Wallraff, and C. Eichler, Rapid high-fidelity multiplexed readout of superconducting qubits, *Phys. Rev. Appl.* **10**, 034040 (2018).

[19] Z. Lin, K. Inomata, K. Koshino, W. Oliver, Y. Nakai

mura, J.-S. Tsai, and T. Yamamoto, Josephson parametric phase-locked oscillator and its application to dispersive readout of superconducting qubits, *Nature communications* **5**, 4480 (2014).

[20] M. Hosoya, W. Hioe, J. Casas, R. Kamikawai, Y. Harada, Y. Wada, H. Nakane, R. Suda, and E. Goto, Quantum flux parametron: a single quantum flux device for josephson supercomputer, *IEEE Transactions on Applied Superconductivity* **1**, 77 (1991).

[21] Y. Yamanashi, T. Matsushima, N. Takeuchi, N. Yoshikawa, and T. Ortlepp, Evaluation of current sensitivity of quantum flux parametron, *Superconductor Science and Technology* **30**, 084004 (2017).

[22] J. A. Grover, J. I. Basham, A. Marakov, S. M. Disseler, R. T. Hinkey, M. Khalil, Z. A. Stegen, T. Chamberlin, W. DeGottardi, D. J. Clarke, J. R. Medford, J. D. Strand, M. J. A. Stoutimore, S. Novikov, D. G. Ferguson, D. Lidar, K. M. Zick, and A. J. Przybysz, Fast, lifetime-preserving readout for high-coherence quantum annealers, *PRX Quantum* **1**, 020314 (2020).

[23] J. C. Pommerening and D. P. DiVincenzo, What is measured when a qubit measurement is performed on a multiqubit chip, *Phys. Rev. A* **102**, 032623 (2020).

[24] M. Khezri, J. Dressel, and A. N. Korotkov, Qubit measurement error from coupling with a detuned neighbor in circuit qed, *Phys. Rev. A* **92**, 052306 (2015).

[25] V. B. Braginsky and F. Y. Khalili, *Quantum measurement* (Cambridge University Press, 1995).

[26] T. Albash and D. A. Lidar, Adiabatic quantum computation, *Rev. Mod. Phys.* **90**, 015002 (2018).

[27] J. Preskill, Quantum computing in the nisq era and beyond, *Quantum* **2**, 79 (2018).

[28] K. Bharti, A. Cervera-Lierta, T. H. Kyaw, T. Haug, S. Alperin-Lea, A. Anand, M. Degroote, H. Heimonen, J. S. Kottmann, T. Menke, W.-K. Mok, S. Sim, L.-C. Kwek, and A. Aspuru-Guzik, Noisy intermediate-scale quantum algorithms, *Rev. Mod. Phys.* **94**, 015004 (2022).

[29] Y. Ji, *Resilience of quantum optimization algorithms*, Ph.D. thesis, Dissertation, Universität Stuttgart, Stuttgart, 2024 (2024).

[30] J. Clarke and A. I. Braginsky, *The SQUID Handbook: Fundamentals and Technology of SQUIDs and SQUID Systems*, Vol. 1 (Wiley-Vch, 2004).

[31] A. J. Berkley, M. W. Johnson, P. Bunyk, R. Harris, J. Johansson, T. Lanting, E. Ladizinsky, E. Tolkacheva, M. H. S. Amin, and G. Rose, A scalable readout system for a superconducting adiabatic quantum optimization system, *Superconductor Science and Technology* **23**, 105014 (2010).

[32] R. Harris, T. Lanting, A. J. Berkley, J. Johansson, M. W. Johnson, P. Bunyk, E. Ladizinsky, N. Ladizinsky, T. Oh, and S. Han, Compound josephson-junction coupler for flux qubits with minimal crosstalk, *Phys. Rev. B* **80**, 052506 (2009).

[33] D. Kafri, C. Quintana, Y. Chen, A. Shabani, J. M. Martinis, and H. Neven, Tunable inductive coupling of superconducting qubits in the strongly nonlinear regime, *Phys. Rev. A* **95**, 052333 (2017).

[34] A. Blais, A. L. Grimsmo, S. M. Girvin, and A. Wallraff, Circuit quantum electrodynamics, *Rev. Mod. Phys.* **93**, 025005 (2021).

[35] E. Jaynes and F. Cummings, Comparison of quantum and semiclassical radiation theories with application to the beam maser, *Proceedings of the IEEE* **51**, 89 (1963).

[36] X. Gu, A. F. Kockum, A. Miranowicz, Y. xi Liu, and F. Nori, Microwave photonics with superconducting quantum circuits, *Physics Reports* **718-719**, 1 (2017), microwave photonics with superconducting quantum circuits.

[37] F. K. Wilhelm, Asymptotic von neumann measurement strategy for solid-state qubits, *Phys. Rev. B* **68**, 060503 (2003).

[38] R. Jozsa, Fidelity for mixed quantum states, *Journal of modern optics* **41**, 2315 (1994).

[39] E. K. Twyeffort Irish, J. Gea-Banacloche, I. Martin, and K. C. Schwab, Dynamics of a two-level system strongly coupled to a high-frequency quantum oscillator, *Phys. Rev. B* **72**, 195410 (2005).